The Self-Assembly of Particles with Isotropic Interactions

by

Kier von Konigslow

A thesis
presented to the University of Waterloo
in fulfillment of the
thesis requirement for the degree of
Master of Science
in
Physics

Waterloo, Ontario, Canada, 2012

I hereby declare that I am the sole author of this thesis. This is a true copy of the thesis, including any required final revisions, as accepted by my examiners.

I understand that my thesis may be made electronically available to the public.

Abstract

In recent years there has been much interest in the self-assembly of materials. Much of this research has been focused on the self-assembly of particles in solution (colloids), typically on the order of nanometres or micrometres in size. While it is easy to imagine the self-assembly of either irregularly shaped particles, or particles under an anisotropic potential, a novel class of colloids with engineerable isotropic interactions have achieved this aim.

With the use of Self-Consistent Field Theory (SCFT), a mean-field model first developed for polymer melt systems, we develop a model for a system of particles of two species. One species experiences a long-range repulsive and short-range attractive interaction. The other is inert, acting as a solvent in which the former is suspended.

Using this method, we calculated the equilibrium morphologies of the system for various parameters including the total volume fraction of one species relative to the other, the strengths and ranges of both the attractive and repulsive components of the interaction, and the relative particle sizes. In this way, we are able to loosely mimic the polymer-coated colloidal systems that are one of the current subjects of self-assembly research.

By reducing our model to a simplified, isotropic interaction, we are able to show that the self-assembly of such systems is the result of the nature of the interaction and not any anisotropy within the model. We have also shown that the phase progressions of this system exhibit remarkable agreement with those of diblock copolymer melt systems despite significant differences in the molecules of these two systems.

Acknowledgements

I would like to thank Dr. Russell Thompson, Dr. Kim Rasmussen, Dr. David Yevick, Dr. Hartwig Peemoeller and Dr. Kostadinka Bizheva for their support. The majority of the computation for this project was accomplished using SHARCNET (WWW.SHARCNET.CA). The code was written using MATLAB (WWW.MATHWORKS.COM).

Table of Contents

List of Figures

List of Abbreviations

AuNP Gold Nanoparticle

BCC Body-Centred Cubic

C Cylinders

DFT Density Functional Theory

FTS Field-Theoretic Simulation

G Gyroid

L Lamella

MC Monte Carlo

MD Molecular Dynamics

NQD Nanocrystal Quantum Dot

OD Optical Density

PL Perforated Lamella

QD Quantum Dot

S Spheres

SCFT Self-Consistent Field Theory

Chapter 1

Introduction

1.1 Motivation

Interest in self-assembly has grown in recent years. For example, block copolymer melt systems have long been known to phase separate into easily controlled micro- and nano-structures based in part on composition. The properties of these materials vary considerably based on the nature of this phase separation. It is of interest that these materials have the ability to form these structures without any need for external interference. While some soft matter materials may exhibit microphase separation in a non-equilibrium situation, albeit with extremely long relaxation times, of particular interest are materials that self-assemble in equilibrium.

Self-assembled materials can have a variety of engineered properties based on the nature of their microstructures, divided into "classical" phases such as Lamella (L) or Body-Centred Cubic (BCC) spheres, and "complex" morphologies such as Perforated Lamella (PL) or the bicontinuous Gyroid (G) phase [59]. Each of these phases can be useful for different properties. A discrete droplet phase is known for its toughness, whereas bicontinuous gyroidal phases can have higher electrical conductivity. The ability to disperse one material within another can also be used to improve the impact characteristics of brittle materials [59].

Colloidal nanoparticles can have many applications due to their interesting properties. These properties can be either optical, electrical or structural in nature [44]. For example, DNA coated gold nanoparticles (AuNPs) have been used to construct arrays of Quantum Dot (QD) "superlattices" fabricated through self-assembly [58]. Such Nanocrystal Quantum Dots (NQDs) also have applications as possible "artificial solids" [22].

Self-Consistent Field Theory (SCFT), pioneered by Edwards, has been a method primarily deployed with polymer melt systems [13, 17, 36, 67, 55, 34]. As a mean-field theory, it has proven to be quite useful in determining equilibrium properties of these systems. Recently, there has been interest in using SCFT outside of this class of systems [67]. In this project, we aim to use SCFT to model a system consisting of two species of interacting particles, one acting as solvent, the other as the colloidal particle of interest. In this way, we will model the self-assembly of these particles.

1.2 Brief Overview

Our model involves two species of particles, labelled A and B. Using the particle density functions of these two species, and beginning with the standard canonical partition function, we derive a set of self-consistent equations used to determine the equilibrium morphologies of these particles under a potential of our own engineering. This potential is designed to parallel the long range repulsion and short range attraction of the systems described above in a loose sense.

By reducing the systems of colloids simulated by others into a purely isotropic model, it is our intention to show that the self-assembly is not a result of any anisotropy within the model but purely a result of the nature of the potential, namely the long-range repulsion and short-range attraction.

We use real-space methods for solving our resulting non-linear self-consistent equations based on methods previously developed for polymer melt systems that do not require us to make any assumptions regarding the symmetries in the equilibrium morphologies of the system. This, combined with our use of random initial conditions, helps to ensure our ability to explore the significant phases of the system.

Chapter 2

Background

2.1 Block Copolymers

The phases of block copolymer melts are of particular interest to this project. A polymer chain is known as a homopolymer if it is made up of one species of monomer. A copolymer, then, is simply a polymer chain made up of more than one species of monomer. Further, if these monomers exist together in sequences, this is known as a block copolymer.

It is easy to imagine that there are many architectures of block copolymers. For example, if there exist two distinct species of monomer, say A and B, then the simplest arrangement would be all A monomers on one side of the chain and all B type on the other. This is known as a diblock copolymer. Of course, triblock and higher order block copolymers are possible.

Triblock copolymers allow for more arrangements of the blocks. For example, the blocks can be arranged in a linear fashion. They can also be arranged in a "star" shape where each block is attached at a single point. Ring configurations are also possible. Higher order block copolymers can have increasingly complex architectures.

In the case of diblock copolymer melt systems, the possible phases are well studied [41, 34]. In such systems, there are three distinct classical phases and several complex phases [36]. The three classical phases are Lamella (L), Cylinders (C), and Spheres (S). The complex phases include Perforated Lamella (PL), Double Diamond (D), and Gyroid (G). Several of these phases are illustrated in Figure 2.1. Matsen et al. discovered experimentally, and confirmed theoretically that the PL phase and the D phase are only metastable, possessing a higher free energy than the G phase [36]. Typically, in the C

phase, the cylinders are arranged in a hexagonal arrangement and in the S phase, the spheres are arranged in a BCC lattice.

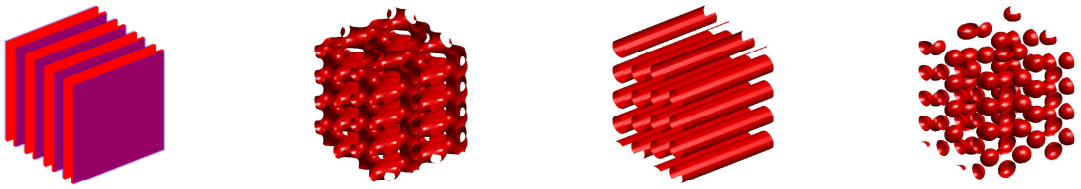

(a) Lamella (b) Gyroid (c) Cylinders (d) Spheres

Figure 2.1: The progression of phases observed as f_A is decreased from $f_A = 0.5$. From $f_A = 0.5$ to $f_A \approx 0.45$, Lamella (L) are observed (a). Near $f_A \approx 0.4$, the system moves to a Gyroid phase (b). From $f_A \approx 0.35$ to $f_A \approx 0.25$, the system enters a Cylindrical (C) phase (c). From $f_A \approx 0.2$ to $f_A \approx 0.15$, the system enters a Spherical (S) phase (d), before finally becoming disordered as $f_A < 0.15$. This result is very similar to the progression of phases for diblock copolymer melts while varying the same parameter. Note that these results were computed using an $L = 8$ sided box. The results have been tiled for clarity.

Block copolymer systems, especially of higher molecular weight, offer many advantages for simulation. Because of the size of the macromolecules, most atomistic effects can be ignored. Fluctuations are also minimized, lending more accuracy to mean-field models [34].

Modelling these systems requires a choice of precision [17]. The most precise, as well as the most costly, would be a fully atomistic computational model. The individual atoms making up the monomers are modelled using quantum mechanics, as well as the interaction potentials between both bonded and non-bonded atoms [17]. The resulting equilibrium state can be determined using either a Monte Carlo (MC) approach or using a Molecular Dynamics (MD) approach [17]. Clearly, this method requires a large amount of computation. For applications dealing with non-atomistic length scales, this approach is not necessary.

Such precise methods can often be approximated using some level of coarse-graining. Yet another approach, known as the bead-spring method, models the polymers as beads connected by springs [17], and once again solves for the equilibrium state using a MD or MC approach. This reduces the problem to two-body interactions and treats the monomers as simple beads, greatly reducing the complexity. The level of complexity can be further reduced by fixing monomers into bead "backbones". The computational requirements remain quite high, so artificially soft repulsions are included. This can lead to some loss of

detail and an unrealistic fluid compressibility [17].

The above approaches remain computationally expensive because of the large numbers of degrees of freedom. It is necessary to track the positions as well as bond angles, etc. of each of the polymers. To simplify calculations further, these degrees of freedom are replaced by density functionals integrated over chemical potential fields, which is the basis for the class of approaches known as the Field-Theoretic Simulations (FTS) [13, 36, 17].

The physics of block copolymers have also been well explored. It is known that amphiphilic block copolymers in solvent will microphase separate [39, 42, 4, 3, 36, 69]. The phase separation comes about due to the amphiphilic nature of the copolymers. Blocks can be chosen such that they are incompatible and prone to phase separation. However, since they are copolymers, macrophase separation is not possible. They can instead microphase separate, taking on a variety of structures. There are three main principles that govern the physical properties of diblock copolymer phase morphologies [34].

The interfacial area per molecule Σ ranks highest in importance of these properties [34]. This is simply defined as the area of the interface divided by the total number of molecules contained by that interface. For diblock copolymers, the free energy contains both an interfacial energy term as well as a stretching term. The interfacial energy term is proportional to Σ whereas the stretching term is proportional to Σ^{-2}. This means that the interfacial term favours a smaller area and the stretching term favours a larger area.

Spontaneous curvature is also an important property [34]. The total volume fraction f of a given block represents the relative lengths of each block. This is true since the melt is composed of polymers with identical block lengths. For an $f = 0.5$ system (or equal block lengths), the system will arrange into flat L sheets. As the fraction is decreased, meaning that the length of one block is larger than the other, the interface will tend to curve towards the species of shorter length.

The last major property is packing frustration [34]. Previous research has indicated that diblock copolymer melts have a tendency to favour constant interfacial curvature. However, in a diblock copolymer system, the blocks have a tendency to want to form brushes of equal length [34]. These two tendencies cannot both be satisfied in most cases, which is known as packing frustration.

2.2 Packing Frustration

Since packing frustration is an important part of the physics of diblock copolymer systems, and is important to the phases presented in this project, it is useful to discuss previous

research in this area.

Intuitively, the L phase does not have packing frustration simply because both the curvature and the brush length are constant throughout [34]. The radius of curvature is infinite throughout and the domains have equal thickness. However, the other phases will experience packing frustration, for example the C phase. This can be illustrated by examining one C phase Wigner-Seitz cell [34], which is hexagonal. The interfacial energy term is satisfied by a perfect cylinder with constant curvature within the cell. However, this requires the polymers in the "majority domain" to stretch to different lengths, which increases the stretching energy term. In order to minimize the stretching energy term, the cylinder would need to take on a more hexagonal shape, as illustrated in Figure 2.2.

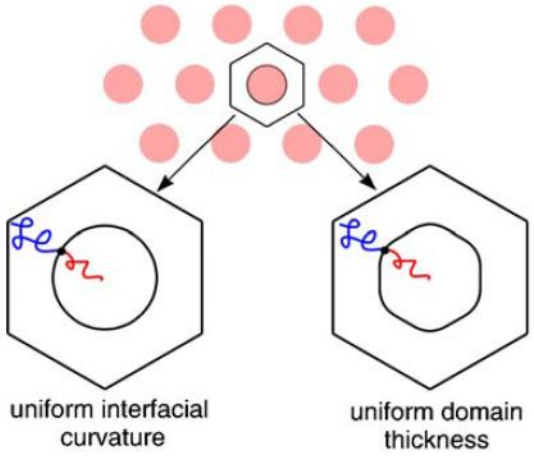

Figure 2.2: Figure showing packing frustration in the cylindrical phase of an amphiphilic diblock copolymer melt system. A uniform interfacial curvature minimizes the interfacial term of the free energy, whereas the uniform thickness of the majority domain minimizes the stretching term of the free energy. In the cylindrical phase of a diblock copolymer system, both of these properties cannot be satisfied at once. From Matsen review [34].

A similar argument can be made for the S phase. The Wigner-Seitz cell in this case is a truncated octahedron. While the spherical interface minimizes the interfacial energy, a geometry closer to the truncated octahedron better satisfies the stretching energy. This is true since both the C and S phases occur only when $f \neq 0.5$, thus the majority domain will tend to dominate the stretching energy term [34].

Matsen et al. determine the amount of packing frustration by measuring the amount of variation in the curvature as well as the variation in domain thickness. The former being

easier to measure, they settled on this as a metric of packing frustration [34]. Using this measure of variation, they are able to analyze the stability of each phase. The PL phase has a high amount of variance, thus a higher packing frustration than the G phase [34].

Matsen, et al. have proposed this packing frustration as a means to explain the metastability of the PL phase. Since the variation in curvature is quite high, they explain that this implies a high packing frustration with PL as opposed to G. They also find that the addition of the majority domain homopolymer can reduce packing frustration, allowing the phase PL to replace G.

2.3 Colloidal Nanoparticles

A colloidal fluid is, in a general sense, a suspension of particles in a medium, either liquid or gas, where the particle sizes are in the nm or μm scale [28]. Particles in this size range are small enough to undergo thermal fluctuation and large enough to overcome sedimentation. Colloids of this type are therefore of interest for self-assembly since they are able to sample configuration space. For example, lock and key colloids (colloids which have been engineered with complimentary shapes that can tunably interlock) take advantage of non-spherical nanoparticles to self-assemble into engineerable structures [56].

Lock and key colloids take advantage of the shape of the particles to induce self-assembly. Sacanna et al. use spherical particles of two different sizes made of silica, poly(methyl methacrylate) or polystyrene. The larger of the two spherical particles, known as the lock particle, is created by nucleating an oil droplet then giving it a polymer shell. The droplet then contracts, buckling the shell in a controlled fashion [56]. The smaller key particles fit into these depressions. The particles are given a short-range attractive potential through the use of the depletion interaction [28].

The range of the interaction between colloids is simply governed by the diameter of the particles. Once two particles come within range of each other, a depletion interaction between the two particles supplies a short-range attraction [56]. This will be discussed in more detail in Section 3.1.2.

Both experimental and theoretical work has shown that polymer grafted nanoparticles suspended in a polymer "matrix" can self-assemble [1]. The group of Ackora, et al. used both a Monte Carlo (MC) and field-theoretic approaches to model the doping of spherical nanoparticles with polymer chains of different lengths and different concentrations. They then attempted to verify their results experimentally. It was found that, similar to amphiphiles, these nanoparticles were capable of self-assembly.

The theory yielded structures including many-particle chains as well as sheets depending on the grafting density. When grafting with polymer chains of increasing length, the particles experienced changes in the type of aggregation. Grafted with dimers, the particles formed long chains, sheets, as well as possible intermediary morphologies. When grafted beyond a critical density, the particles no longer agglomerate but simply disperse.

Their subsequent experimental techniques, using 14-nm spherical silica particles that had been grafted to polystyrene in a polystyrene matrix, confirmed the theoretical results. The particles, when ungrafted, formed large ($\sim 1-100\mu m$) spherical clusters, as expected.

Polymers can be attached to the surface of a colloid in three ways [28]. They can attach to the surface at one end of the polymer chain. At low packing densities, the chain will tend not to stretch to its full length (since that would decrease entropy) and will form a mushroom shape. At higher packing densities, the chains will tend to spread out, forming a brush. Finally, the chains do not have to attach at one end, but may attach to the surface at random points along its chain.

The behaviour of the attached polymers depends highly on the quality of the solvent. In a poor solvent, the polymers will tend to aggregate and collapse, as they want to minimize contact with the solvent [28]. On the contrary, in a good solvent, the polymers will tend to repel and stretch. This has a correspondingly profound effect on the colloids to which they are attached.

In a good solvent, the polymers will repel, essentially causing the colloids to repel as well. DNA can be used to customize the inter-colloid interaction [11, 33, 44, 57, 58, 66], allowing the customization of a short-range attraction between colloids using an unpaired "sticky" end of a DNA strand.

Recent research has indicated that nanoparticles grafted with customized DNA brushes are capable of self-assembly [65, 11]. Larger nano-particles and micro-particles are well suited to self-assembly since they are both large enough to allow optical imaging and small enough to undergo thermal fluctuations, which will be described in more detail in Section 3.1.

Tindemans et al. constructed a model of DNA-coated colloid systems using a regular lattice, each lattice site being occupied by a particle of type A, B, C, etc. [65] In this way, they could customize the nature and range of each inter-particle interaction with nearest-neighbour, next-nearest-neighbour, etc. range. This was done for both a square lattice and a triangle lattice in 2-dimensions.

They argue that for a specific pattern to be a ground state, it must be lower in energy than every distinguishable configuration or symmetry (based on the symmetries of

the lattices) [65]. They define $n(0)$ as no-interaction, $n(1)$ as a nearest-neighbour range interaction, $n(2)$ as a next-nearest-neighbour range interaction, etc...

Based on these ideas, they are able to put a lower bound on the range of interaction required to design non-trivial patterns for a given lattice. They found this minimum range to be $n(2)$ for a triangular lattice and $n(3)$ for a square lattice [65]. One of their prescriptions for a designable pattern consists of an attractive interaction of range $n(1)$ and a repulsive interaction of range $n(2)$ for a triangular lattice. The repulsive interaction is extended to $n(3)$ for the square lattice [65]. They used a Monte Carlo approach on both square and triangular lattices to test their assertions, finding that indeed long range patterns of many particle species were engineerable in this way [65].

In experiments with DNA-grafted nanoparticles, Dreyfus et al. performed an experiment in which roughly 2.2×10^4 DNA molecules were coated to the surface of $525nm$ particles. The DNA strands used consisted of a bottom segment of 49 double-strand base pairs with a top segment of 11 single-strand bases [11]. The top end of the DNA molecule was thus engineered to be "sticky". They found that below a critical temperature T_d, the nanoparticles would begin to aggregate as illustrated in Figure 2.3.

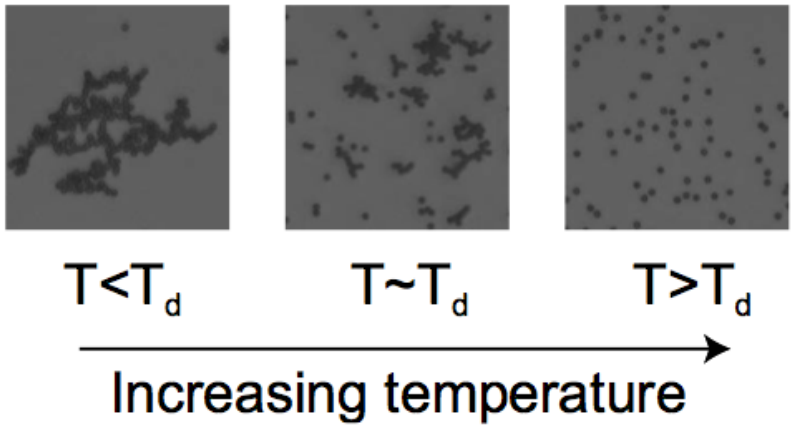

Figure 2.3: Figure showing the aggregation and disaggregation of DNA-coated polystyrene particles across a critical temperature T_d. Below T_d (left) the particles aggregate into larger structures. Near T_d (center), singlet particles and aggregates coexist at equilibrium. Above T_d (right), particles remain as singlets. From Dreyfus et al. [11]

In order to measure the aggregation, they proposed measuring the Optical Density (OD), since the single-stranded DNA will absorb more UV light than the double-stranded

DNA. In this way, it was possible to estimate the DNA hybridization and thus the number of singlet particles present. They found that the dissociation temperature was highly dependent on the DNA surface density. The dissociation curves were also very sharp, with a well defined dissociation temperature T_d [11].

Dreyfus et al. further postulate that their DNA-nanoparticle colloid self-assembly method could also be used on noble-metals such as silver or platinum, as well as on semiconductor nanoparticles such as CdSe or CdS.

Chapter 3

Theory

3.1 Colloids

3.1.1 Sedimentation Length

As discussed previously, colloids are simply suspensions of particles within a fluid. Intuitively, without fluctuation the colloid would be unable to move through the possible particle configurations. It would simply be trapped in its initial configuration. Fluctuation, therefore, is essential to self-assembly.

This fluctuation is brought about by the Brownian motion of the particles in the fluid. The energy scale of these thermal fluctuations scales with temperature. The sedimentation length l_{sed} is defined as the ratio of the thermal energy to the force of gravity [28]

$$l_{sed} = \frac{k_B T}{m^* g} \tag{3.1}$$

where m^* is the effective mass of a colloid particle due to buoyancy and is given by $m^* = v_c \Delta\rho$, v_c is the volume occupied by a colloid particle, and $\Delta\rho$ is the difference in density between a colloidal particle and the solvent.

A colloid is said to be Brownian when the sedimentation length is roughly equal to the size of a particle, or when $l_{sed} \approx \sqrt[3]{v_c}$ [28].

3.1.2 Depletion Interaction

The depletion interaction is an important consideration in colloidal systems [28]. The depletion interaction is a short-range attraction that is a function of the solvent in which the colloid is suspended [28, 56]. The principle applies equally to colloids suspended in a polymer solution.

Define r_p as the radius occupied by an unstretched polymer in solution [56]. For any polymer within r_p. The depletion layer surrounding a particle is defined as a layer of thickness r_p. Any polymer within this layer will experience a loss of configurational entropy due to the excluded volume of the particle.

For an isolated particle, this leads to an isotropic osmotic pressure [28]. However, when the depletion layers of two particles overlap, there is an imbalance in this pressure. The forces involved are purely repulsive, but the net effect is an attractive force between the two particles. The depletion layers will begin to overlap when the two particles come within a distance of $2r_p$ of each other, effectively setting this as the length-scale of the interaction.

3.2 Model

3.2.1 Densities

The particle *density function* for a given species s can be written as:

$$\hat{\Phi}_s(\mathbf{r}) \equiv v_s \sum_{i=1}^{N_s} d\mathbf{r}\delta(\mathbf{r} - \mathbf{r}_{i,s}) \tag{3.2}$$

where $\mathbf{r}_{i,s}$ is the position of particle i, N_s is the number of particles of species s, and v_s is a normalization constant. This definition of the density function assumes that the particle i is localized entirely at the position $\mathbf{r}_{i,s}$.

While it is convenient to imagine the density function this way, the following arguments are also valid for a smoothed density function that represents the volume fraction of species s at the point $\mathbf{r}$. It should be noted that I will be referring to the volume fraction function (the smoothed version of the above) as a density function. Since much of the literature uses density functions, it is easier to maintain continuity.

Assuming that the particles are confined to a volume V, then the total volume occupied

by a particular species s must be the integral of its density over all space.

$$\int \hat{\Phi}_s(\mathbf{r})d\mathbf{r} = \int v_s \sum_{i=1}^{N_s} d\mathbf{r}\delta(\mathbf{r} - \mathbf{r}_{i,s}) = N_s v_s = f_s V \tag{3.3}$$

This indicates that the normalization constant v_s is the volume of a particle of species s. A *total volume fraction* f_s can also be defined as the fraction of volume V that all of the s-species particles occupy.

Moving to a two species system, it is convenient to define $v_A \equiv v_0$ as the volume occupied by an A-species particle and $v_B \equiv \alpha v_0$ to be the volume occupied by a B-species particle. In this way, the relative particle size

$$\frac{v_B}{v_A} = \alpha \tag{3.4}$$

is the ratio of the volumes of a B-species particle to an A-species particle.

3.2.2 Interaction Potential

The potential U is a function of the positions of all of the particles in the system.

$$U(\{\mathbf{r}_A\}, \{\mathbf{r}_B\}, \{\mathbf{r}_C\}, ...) = U\left[\hat{\Phi}_A, \hat{\Phi}_B, \hat{\Phi}_C, ...\right] \tag{3.5}$$

where $\{\mathbf{r}_s\}$ represents the set of all position vectors $\mathbf{r}$ of particles of species s.

Now, it is necessary to define the potential functional in order to calculate the potential of the system for a given set of density distribution functions as defined in Equation 3.2. For the purposes of this model, only two-particle interactions will be considered.

There exist three possible two-particle interactions in the two-species system: $U_{AA}(r)$, $U_{AB}(r)$ and $U_{BB}(r)$ which are functions of the separation between particles. These potentials correspond to the A-A interactions, A-B interactions, and B-B interactions respectively. The potential of the system due to these inter-particle interactions is expressed

as

$$U(\{\mathbf{r}_A\},\{\mathbf{r}_B\}) = \sum_{i=1}^{N_A}\sum_{j<i} U_{AA}(|\mathbf{r}_i-\mathbf{r}_j|) + \sum_{i=1}^{N_A}\sum_{j=1}^{N_B} U_{AB}(|\mathbf{r}_i-\mathbf{r}_j|) + \sum_{i=1}^{N_B}\sum_{j<i} U_{BB}(|\mathbf{r}_i-\mathbf{r}_j|) \quad (3.6)$$

which, using Equation 3.2, reduces to an integral on the density functions Φ_A and Φ_B.

$$U[\hat{\Phi}_A,\hat{\Phi}_B] = \int\int d\mathbf{r}d\mathbf{r}'\Bigg(\frac{1}{2v_0^2}\hat{\Phi}_A(\mathbf{r})U_{AA}(|\mathbf{r}-\mathbf{r}'|)\hat{\Phi}_A(\mathbf{r}') + \frac{1}{\alpha v_0^2}\hat{\Phi}_A(\mathbf{r})U_{AB}(|\mathbf{r}-\mathbf{r}'|)\hat{\Phi}_B(\mathbf{r}') + \frac{1}{2\alpha^2 v_0^2}\hat{\Phi}_B(\mathbf{r})U_{BB}(|\mathbf{r}-\mathbf{r}'|)\hat{\Phi}_B(\mathbf{r}')\Bigg) \quad (3.7)$$

3.2.3 Partition Function

It is now possible to write down the Hamiltonian of the system. For a system of N_s interacting particles of species s, the classical Hamiltonian can be expressed as

$$\mathcal{H} = \sum_{i=1}^{N_s}\frac{\mathbf{p}_i^2}{2m} + \frac{1}{2}\sum_{i=1}^{N_s}\sum_{j=1}^{N_s} U(\mathbf{r}_i-\mathbf{r}_j) \quad (3.8)$$

It should be noted that in the above sum, the terms $i=j$ represent self-interactions. These terms have been retained since, in the following computation of the partition function Z and free energy F of the system, the contribution of these terms will not be relevant. In the canonical ensemble, with a fixed number of particles N, this factor is a constant and can be ignored in energy calculations.

It can be shown that for a classical system of N interacting particles confined to a volume, the canonical ensemble, the partition function is [52]

$$Z_N(T,V) = \frac{1}{N!h^{3N}}\int\int d\mathbf{r}^N d\mathbf{p}^N e^{-\beta\left(\sum_{i=1}^N \frac{\mathbf{p}_i^2}{2m} + \frac{1}{2}\sum_{i=1}^N\sum_{j=1}^N U(|\mathbf{r}_i-\mathbf{r}_j|)\right)} \quad (3.9)$$

Assuming that species A particles interact with each-other with potential $U_{AA}(\mathbf{r})$ and

species B particles are non-interacting, then the partition function for the combined system is simply the product of the two separate partition functions. Define $N = N_A + N_B$

$$Z_N(T,V) = \frac{1}{N_A! N_B! h^{3N}} \times \int d\mathbf{r}_A^{N_A} d\mathbf{r}_B^{N_B} d\mathbf{p}_A^{N_A} d\mathbf{p}_B^{N_B} e^{-\beta\left(\sum_{i=1}^{N_A} \frac{\mathbf{p}_{A,i}^2}{2m} + \sum_{i=1}^{N_B} \frac{\mathbf{p}_{B,i}^2}{2m} + \frac{1}{2}\sum_{i=1}^{N_A}\sum_{j=1}^{N_A} U_{AA}(|\mathbf{r}_{A,i} - \mathbf{r}_{A,j}|)\right)} \tag{3.10}$$

For particles in the classical regime, the momentum dependent portion of the partition function is characterized by the thermal wavelength [52] λ_T.

$$\lambda_T = \left(\frac{2m\hbar^2}{mk_BT}\right)^{1/2} \tag{3.11}$$

Thus Equation 3.10 becomes

$$Z_N(T,V) = \frac{1}{N_A! N_B! \lambda_{T,A}^{3N_A} \lambda_{T,B}^{3N_B}} \int d\mathbf{r}_A^{N_A} d\mathbf{r}_B^{N_B} e^{-\frac{\beta}{2}\sum_{i=1}^{N_A}\sum_{j=1}^{N_A} U(|\mathbf{r}_{A,i} - \mathbf{r}_{A,j}|)} \tag{3.12}$$

It is now desirable to rewrite the partition function as a functional integral. It is necessary to introduce the functional identity [17] $\int \mathcal{D}\Phi\ \delta(\Phi - \hat{\Phi}) = 1$. Equations 3.6 and 3.7 allow the potential term of the Hamiltonian to be rewritten in terms of the density functions Φ_A and Φ_B.

$$Z_N(T,V) = \frac{1}{N_A! N_B! \lambda_{T,A}^{3N_A} \lambda_{T,B}^{3N_B}} \times \int d\mathbf{r}_A^{N_A} d\mathbf{r}_B^{N_B} \int \mathcal{D}\Phi_A \mathcal{D}\Phi_B \delta(\Phi_A - \hat{\Phi}_A)\delta(\Phi_B - \hat{\Phi}_B) e^{-\frac{\beta\sigma^6}{2v_0^2}\int \frac{d\mathbf{r}}{\sigma^3}\frac{d\mathbf{r}'}{\sigma^3}\hat{\Phi}_A(\mathbf{r})U_{AA}(|\mathbf{r}-\mathbf{r}'|)\hat{\Phi}_A(\mathbf{r}')} \tag{3.13}$$

where we define σ to be an arbitrary length-scale in order to render the contents of the exponential dimensionless. The choice of length-scale will be discussed in greater detail later on.

In order to continue it is convenient to introduce the real fields $W_A(\mathbf{r})$ and $W_B(\mathbf{r})$, which are interpreted as chemical potential fields. We are free to choose the delta functional δ,

which we can express as [17]

$$\delta\left(\Phi-\hat{\Phi}\right)=\int_{-i\infty}^{+i\infty}\mathcal{D}W\exp\left[\int\frac{d\mathbf{r}}{\sigma^3}\,W\left(\mathbf{r}\right)\left(\Phi-\hat{\Phi}\right)\right] \tag{3.14}$$

leading to a functional form of the partition function integrated over all possible density functions and fields. It is now possible to define the term Q_s as

$$\begin{aligned}\int\frac{d\mathbf{r}_s^{N_s}}{\sigma^{3N_s}}\,\exp\left(-\int\frac{d\mathbf{r}}{\sigma^3}W_s(\mathbf{r})\hat{\Phi}_s(\mathbf{r})\right)&=\int\frac{d\mathbf{r}_s^{N_s}}{\sigma^{3N_s}}\,\exp\left(-\frac{v_s}{\sigma^3}\sum_{i=1}^{N_s}W_s(\mathbf{r}_{i,s})\right)\\&=\left(\int\frac{d\mathbf{r}}{\sigma^3}\,\exp[-\frac{v_s}{\sigma^3}W_s(\mathbf{r})]\right)^{N_s}\equiv Q_s^{\frac{f_sV}{v_s}}\end{aligned} \tag{3.15}$$

where we have expressed the number of particles of specied s as $N_s=\frac{f_sV}{v_s}$. This allows for the further simplification of Equation 3.13, which can now be written as a functional integral of chemical potential fields as well as densities.

$$\begin{aligned}&Z_N(T,V)=\frac{1}{N_A!N_B!\lambda_{T,A}^{3N_A}\lambda_{T,B}^{3N_B}}\\&\times\int\mathcal{D}\Phi_A\mathcal{D}\Phi_B\int\mathcal{D}W_A\mathcal{D}W_BQ_A^{\frac{f_AV}{v_0}}Q_B^{\frac{f_BV}{\alpha v_0}}\;e^{-\frac{\beta\sigma^6}{2v_0^2}\int\frac{d\mathbf{r}}{\sigma^3}\frac{d\mathbf{r}'}{\sigma^3}\Phi_A(\mathbf{r})U_{AA}(|\mathbf{r}-\mathbf{r}'|)\Phi_A(\mathbf{r}')+\int\frac{d\mathbf{r}}{\sigma^3}W_A(\mathbf{r})\Phi_A(\mathbf{r})+W_B(\mathbf{r})\Phi_B(\mathbf{r})}\end{aligned} \tag{3.16}$$

which has the form

$$Z_N(T,V)\propto\int\mathcal{D}\Phi\int\mathcal{D}W\;\exp\left(-\beta\mathcal{H}\left[\Phi,W\right]\right) \tag{3.17}$$

3.2.4 Saddle Function Approximation and Free Energy

The saddle-function approximation, also known as the method of steepest descent [10] provides an approximation for further simplifying the partition function in Equation 3.16. It is possible to approximate the integral by expanding the action about some $\phi(\mathbf{r})$ and

$w(\mathbf{r})$ that minimize the Hamiltonian.

$$\left.\frac{\delta\mathcal{H}[W(\mathbf{r})]}{\delta W(\mathbf{r})}\right|_{W(\mathbf{r})=w(\mathbf{r})} = 0 \tag{3.18}$$

$$\left.\frac{\delta\mathcal{H}[\hat{\Phi}(\mathbf{r})]}{\delta\hat{\Phi}(\mathbf{r})}\right|_{\hat{\Phi}(\mathbf{r})=\phi(\mathbf{r})} = 0 \tag{3.19}$$

The drawback to using this method is that it does not take into account any fluctuation in these functions. This method assumes that there exists a unique global minimum [2]. Typically, this is not the case, since local minima known as metastable states may well exist. This approximation also does not make any assertion as to how the system can achieve this state. Using this approximation, the integral can be approximated using

$$\begin{aligned} Z_N(T,V) \approx & \frac{1}{N_A!N_B!\lambda_{T,A}^{3N_A}\lambda_{T,B}^{3N_B}} \\ & \times Q_A^{\frac{f_AV}{v_0}} Q_B^{\frac{f_BV}{\alpha v_0}} \; e^{-\frac{\beta\sigma^6}{2v_0^2}\int\frac{d\mathbf{r}}{\sigma^3}\frac{d\mathbf{r}'}{\sigma^3}\phi_A(\mathbf{r})U_{AA}(|\mathbf{r}-\mathbf{r}'|)\phi_A(\mathbf{r}')+\int\frac{d\mathbf{r}}{\sigma^3}w_A(\mathbf{r})\phi_A(\mathbf{r})+w_B(\mathbf{r})\phi_B(\mathbf{r})} \end{aligned} \tag{3.20}$$

where Q_A and Q_B are now functions of w_A and w_B respectively.

With the partition function of the canonical ensemble in hand, it is now possible to calculate the Helmholtz free energy of the system using the relation $F = -k_BT\ln Z_N(V,T)$. This leads to the following free energy

$$\begin{aligned} \frac{F}{k_BT} = & -\ln\left(\frac{1}{N_A!N_B!\lambda_{T,A}^{3N_A}\lambda_{T,B}^{3N_B}}\right) - \frac{f_AV}{v_0}\ln Q_A - \frac{f_BV}{\alpha v_0}\ln Q_B \\ & + \frac{\sigma^6}{2v_0^2}\int\frac{d\mathbf{r}}{\sigma^3}\frac{d\mathbf{r}'}{\sigma^3}\phi_A(\mathbf{r})\frac{U_{AA}\left(|\mathbf{r}-\mathbf{r}'|\right)}{k_BT}\phi_A(\mathbf{r}') - \int\frac{d\mathbf{r}}{\sigma^3}w_A(\mathbf{r})\phi_A(\mathbf{r}) + w_B(\mathbf{r})\phi_B(\mathbf{r}) \end{aligned} \tag{3.21}$$

Rather than introduce incompressibility strictly, which can be expressed as $\phi_A(\mathbf{r}) + \phi_B(\mathbf{r}) = 1$, it is possible to introduce an energy penalty for incompressibility violation. This energy penalty can be controlled by adding an incompressibility parameter $\hat{\kappa}$. The free energy derived above is an extensive property. It is useful in the bulk case to deal with an intensive free energy by dealing with the free energy per unit volume. Since the length-scale σ is arbitrary, it is convenient to define it as the "size" of a particle of species

A. Let $\sigma = \sqrt[3]{v_0}$.

$$\frac{v_0 F}{k_B T V} = -\frac{v_0}{V}\ln\left(\frac{1}{N_A! N_B! \lambda_{T,A}^{3N_A}\lambda_{T,B}^{3N_B}}\right) - f_A \ln\left(Q_A[w_A(\mathbf{r})]\right) - \frac{f_B}{\alpha}\ln\left(Q_B[w_B(\mathbf{r})]\right)$$
$$+ \frac{v_0}{2V}\int \frac{d\mathbf{r}}{v_0}\frac{d\mathbf{r}'}{v_0}\phi_A(\mathbf{r})\frac{U_{AA}\left(|\mathbf{r}-\mathbf{r}'|\right)}{k_B T}\phi_A(\mathbf{r}') - \frac{v_0}{V}\int \frac{d\mathbf{r}}{v_0} w_A(\mathbf{r})\phi_A(\mathbf{r}) + w_B(\mathbf{r})\phi_B(\mathbf{r})$$
$$+ \frac{\hat{\kappa}}{2}\int \frac{d\mathbf{r}}{v_0}(\phi_A(\mathbf{r}) + \phi_B(\mathbf{r}) - 1)^2 \quad (3.22)$$

where Q_A and Q_B are, from Equation 3.15, defined as

$$Q_A = \int \frac{d\mathbf{r}}{v_0} e^{-w_A(\mathbf{r})} \quad (3.23)$$
$$Q_B = \int \frac{d\mathbf{r}}{v_0} e^{-\alpha w_B(\mathbf{r})} \quad (3.24)$$

3.2.5 Self-Consistent Equations

The final intensive form of the free energy in Equation 3.22 is a functional of four functions: $\phi_A(\mathbf{r})$, $\phi_B(\mathbf{r})$, $w_A(\mathbf{r})$, and $w_B(\mathbf{r})$, which are the two density functions and the two chemical potential fields, respectively.

It should be noted that the saddle-function approximation mentioned in the previous section requires these functions to be the functions that *minimize the action*. This can be accomplished by finding the functions that minimize the free energy. By taking the functional derivative of Equation 3.22 with respect to each of densities and fields and setting them to zero, it is possible to obtain four self-consistent equations.

$$\phi_A(\mathbf{r}) = \frac{f_A V}{v_0 Q_A} e^{-w_A(\mathbf{r})} \quad (3.25)$$
$$\phi_B(\mathbf{r}) = \frac{f_B V}{v_0 Q_B} e^{-\alpha w_B(\mathbf{r})} \quad (3.26)$$
$$w_A(\mathbf{r}) = \int \frac{d\mathbf{r}'}{v_0}\phi_A(\mathbf{r}')\frac{U_{AA}\left(|\mathbf{r}-\mathbf{r}'|\right)}{k_B T} + \hat{\kappa}(\phi_A(\mathbf{r}) + \phi_B(\mathbf{r}) - 1) \quad (3.27)$$
$$w_B(\mathbf{r}) = \hat{\kappa}(\phi_A(\mathbf{r}) + \phi_B(\mathbf{r}) - 1) \quad (3.28)$$

3.2.6 Expression of Potential

The free energy expression in Equation 3.22 applies for a general potential $U(r)$. The potentials of interest to research into self-assembly exhibit characteristic properties. In contrast to the more standard inter-particle interactions, such as the Lennard-Jones 6-12 potential, these potentials feature an attraction at short-range and a repulsion at long range.

In addition to the attraction-repulsion requirements, the potential should feature key properties. In Section 3.2.2 the nature of the interaction potential was described in rough detail as being only a function of the separation between particles, implying this potential is characteristic of a conservative force. It follows then that the potential must be not only continuous, but continuously differentiable as a function of separation r.

At first we tried to simply flip the Lennard-Jones potential but this was not a satisfactory solution for several reasons. As the separation distance approaches $r \to 0$, the Lennard-Jones potential approaches positive infinity. This singularity is useful in enforcing an excluded volume; as the separation between particles becomes small, the situation becomes increasingly energetically unfavourable. Flipping this potential would result flipping the singularity into an attraction, which is not desirable. A possible solution would be a linear shift of the potential along the separation r axis. However, this would create a cusp at $r = 0$ resulting in a potential $U(r)$ that is not differentiable at the point $r = 0$.

The next solution we tried was to create a potential by superimposing two Gaussians representing the attractive and repulsive regions. For example, an inverted Gaussian centred about the origin and a positive Gaussian centred at some $r = \lambda$. Such a potential would have the form

$$\frac{\sigma^3 U(r)}{v_0 k_B T} = -A_1 \exp\left(-\frac{r^2}{\sigma^2}\right) + A_2 \exp\left(-\frac{(r-\lambda)^2}{\sigma^2}\right) \tag{3.29}$$

where A_1 and A_2 determine the depth of the potential well and the height of the potential barrier, respectively. λ represents the position of the repulsive region, effectively controlling the length-scale of the attractive and repulsive regions.

The potential in Equation 3.29 is simple and meets several requirements. During the computation of the fixed points of the SCFT equations, it is necessary to discretize the potential. Should the potential contain a singularity, the nature of the potential would change depending on the discretization. Since Equation 3.29 contains no singularities, it is clear that the potential is continuous on the interval $(0, +\infty]$.

Problems began to arise as the limits are analysed. Ideally, the two Gaussians that form the potential should be quite independent. The depth of the potential well A_1 should not be affected by the height of the potential barrier A_2. However, the limit $\lim_{r\to 0} \frac{\sigma^6 U(r)}{v_0^2 k_B T} = -A_1 + A_2 \exp\left(-\frac{\lambda^2}{\sigma^2}\right)$ indicates that the depth of the potential well is indeed coupled to the height of the potential barrier. Using a similar argument, the height of the potential barrier is also coupled to the depth of the potential well, making these parameters very difficult to control independently.

Next, it is necessary that the potential of a conservative force be differentiable over its domain. At first glance, the potential in Equation 3.29 may seem differentiable, but problems arise at $r \to 0$. Since later computations are done in Cartesian space, and since the mapping $r : (x, y, z) \to r(x, y, z)$ is itself not differentiable at $r = 0$, it is necessary to look at the potential in the cartesian coordinate system. A simple calculation reveals that the partial derivatives with respect to the coordinates x, y, z respectively do not exist at the origin; the limit $\lim_{x\to 0^+} \left.\frac{\partial U(x,y,z)}{\partial x}\right|_{y=0,z=0} = \frac{2A_2\lambda}{\sigma^2} \exp\left(-\frac{\lambda^2}{\sigma^2}\right)$ whereas $\lim_{x\to 0^-} \left.\frac{\partial U(x,y,z)}{\partial x}\right|_{y=0,z=0} = -\frac{2A_2\lambda}{\sigma^2} \exp\left(-\frac{\lambda^2}{\sigma^2}\right)$. This implies that the potential is not differentiable at the origin, since no Jacobian can be calculated at this point. Without being everywhere differentiable, the Gaussian potential is not acceptable as the characteristic potential of a conservative inter-particle force.

With the requirements for an acceptable potential outlined, it is possible to generate an appropriate potential. The potential we have chosen for our purposes can be expressed as a piecewise function.

$$\frac{\sigma^3 U(r)}{v_0 k_B T} = \begin{cases} -\frac{(A_1+A_2)}{2} \cos\left(\frac{\pi r}{\lambda}\right) - \frac{(A_1-A_2)}{2} & , \text{for } r \leq \lambda \\ A_2 \exp\left(-\frac{(r-\lambda)^2}{2\gamma^2}\right) & , \text{for } r > \lambda \end{cases} \tag{3.30}$$

where A_1 and A_2 are dimensionless quantities corresponding to the depth of the potential well and the height of the potential barrier respectively and γ controls the width of the potential barrier. Figure 3.1 plots the new potential as a function of the relative separation r between two particles.

Quick examination of this potential reveals that it meets the aforementioned criteria. The new potential is continuous, differentiable everywhere including at the origin, does not contain any singularities, and most importantly contains the desired two length-scale interaction. Further, the regions of attraction and repulsion can be controlled *independently*

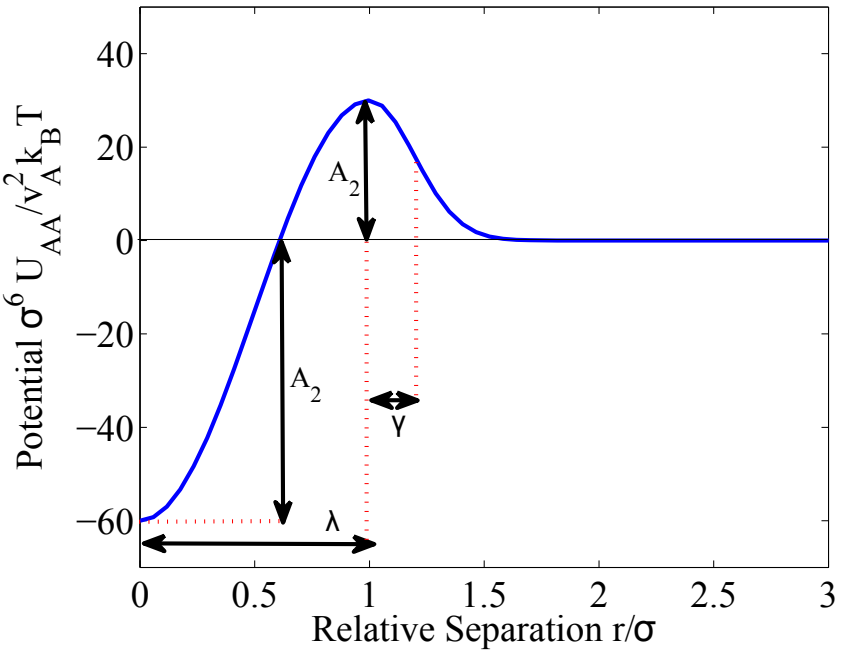

Figure 3.1: A plot of the isotropic inter-particle potential, which features long-range repulsion and short-range attraction, as a function of particle separation. A weak excluded volume is enforced through incompressibility, not through the potential itself.

using their respective parameters.

3.3 Algorithm

In order to solve the self-consistent equations in Section 3.2.5, a method is required to search density space in order to find a fixed-point. In order to minimize the free energy, a density function must be found that satisfies all of the equations. This is not trivial since the equations are self-consistent.

The most obvious method would be to search density space by somehow randomly sampling configurations. Approaches may even be designed to mimic a Monte Carlo algorithm. The drawback to this approach is that it would be extremely computationally demanding and inefficient. A more systematic approach is appropriate.

There are two main classes of methods for solving the SCFT equations. They fall into Spectral (Fourier space) and Real Space methods [17]. Each of these methods present different strengths and weaknesses.

The Spectral methods, pioneered by Matsen and Schick, involves computing the field functions in a Fourier basis. This Fourier basis is composed of functions which must satisfy two requirements [17]; the functions must be eigenfunctions of the Laplacian operator, and they must also have the same symmetries as the phase of the fluid at the saddle-point. This requires some fore-knowledge of the phases being sought. The Fourier expansion of the fields is typically truncated after a given number of terms, the number of which dictates the computational cost of solving the equations. The obvious drawback of the Matsen-Schick method is that it requires some foreknowledge of the symmetries. For example, in the diblock copolymer case, there exist a relatively small number of morphologies which can be used to calculate these basis functions. A comparison of the relative free energies of these morphologies for a given set of parameters allows the selection of a particular state over another [17]. However, for more complex systems such as copolymers with greater number of components, these symmetries may be more complicated and less clear. The symmetries not being known in the colloidal systems being investigated, it was decided not to use the spectral approaches.

It is worth going into greater detail regarding the Real Space methods, since they are favoured in this project. Early real-space methods, such as the method developed by Helfand and Wasserman, attempted to use symmetry to reduce the problem to a single dimension [17]. Again, as it was not advantageous to reduce the problem to a finite number of known phases, these approaches were not selected.

It is possible to iterate on either the fields $w(\mathbf{r})$ or the densities $\phi(\mathbf{r})$. For our purposes, it was decided to iterate on the density functions. The recursion equation that gives rise to the algorithm can be expressed as

$$\phi^{k+1}(\mathbf{r}) = (1-\rho)\phi^{k}(\mathbf{r}) + \rho\phi^{k+1/2}(\mathbf{r}) \tag{3.31}$$

where k is the current iteration and $k+1/2$ represents the new density function calculated by using the SCFT equations 3.25 - 3.28 and ρ is the mixing parameter, representing how much of the new function should be mixed with the old to put into the next iteration. The superscripts in this section denote iteration.

The algorithm proceeds as follows: for a density function ϕ_A^k, it is possible to calculate the corresponding chemical potential field w_A^k. Using incompressibility, this choice of ϕ_A^k density implies a unique ϕ_B^k that likewise allows calculation of the field $w_B^{k+1/2}$. Since the

equations are self-consistent, the densities $\phi_A^{k+1/2}$ and $\phi_B^{k+1/2}$ can then be calculated using these fields. Should the new A and B densities match the old ones to some tolerance, the densities represent a fixed point and the process is finished. If not, then the densities are mixed according to Equation 3.31.

3.4 Computation

In order to implement the algorithm represented by Equation 3.31, the volume must be "sampled" as a finite lattice. A balance between resolution and computation was achieved using a lattice of $64 \times 64 \times 64$ data points. System size was chosen to be large enough to minimize finite size effects while small enough to allow for a reasonable resolution. Using the rough length-scale $\sqrt[3]{v_0}$, box sizes were chosen to be $L = 8, 10, 15$ per side.

In this section, superscripts represent iteration. The initial guess for the density function $\phi_A^0(\mathbf{r})$ was chosen randomly using a Gaussian random number generator with mean f_A and standard deviation of 0.15. In this way, the density would fluctuate about the volume average f_A, in order that no single phase would be consistently favoured over the others because of the initial conditions. Since the system should obey incompressibility, the B particle density was simply chosen to be $\phi_B^0(\mathbf{r}) = 1 - \phi_A^0(\mathbf{r})$.

It is helpful to consider Fourier space at this point in order to calculate the interaction term of Equation 3.27. In this way, it is possible to take advantage of the *Convolution Theorem* of Fourier transforms. The theorem states that the Fourier transform of the convolution of functions f and g, denoted $(f \circ g)(\mathbf{r}) = \int_{\mathbb{R}^3} d\mathbf{r}' f(\mathbf{r}')g(\mathbf{r}-\mathbf{r}')$ into the frequency domain becomes the point-wise product of functions $\tilde{f}(\boldsymbol{\xi})\tilde{g}(\boldsymbol{\xi})$ and conversely the Fourier transform of the product of functions $f(\mathbf{r})g(\mathbf{r})$ into the frequency domain becomes the convolution$(\tilde{f} \circ \tilde{g})(\boldsymbol{\xi})$. Exploiting this theorem, the integral becomes

$$\int d\mathbf{r}' \phi_A(\mathbf{r}') U_{AA}(\mathbf{r} - \mathbf{r}') = (\phi_A \circ U_{AA})(\mathbf{r}) = \mathcal{F}\left[(\tilde{\phi}_A \tilde{U}_{AA})(\boldsymbol{\xi})\right] = \mathcal{F}\left[\tilde{\phi}_A(\boldsymbol{\xi})\tilde{U}_{AA}(\boldsymbol{\xi})\right] \quad (3.32)$$

which greatly simplifies the procedure. The integral simply becomes the point-wise product of the Fourier transform of the two functions, which can then be transformed to real-space once again.

Once the integral in Equation 3.27 has been calculated, it is trivial to calculate the fields w_A^0 and w_B^0 in order to implement the recursion in Equation 3.31. Assuming that the guess is not a fixed point, the field, once plugged into Equations 3.25 and 3.26, will

produce a new set of densities $\phi_A^{1/2}$ and $\phi_B^{1/2}$. Point-wise mixing the old and new densities with mixing parameter ρ will generate a new guess for the densities.

At each step, the relative divergence is estimated. This is done by computing the square of the relative L_2 norm of the difference between ϕ_A^k and $\phi_A^{k+1/2}$ using the equation

$$\text{divergence} \equiv \frac{\int \frac{d\mathbf{r}}{v_0} \left(\phi_A^{k+1/2}(\mathbf{r}) - \phi_A^k(\mathbf{r})\right)^2}{\int \frac{d\mathbf{r}}{v_0} \left(\phi_A^k(\mathbf{r})\right)^2} \tag{3.33}$$

which can easily be computed in real space. In essence, this is a measure of whether or not the fields going into the algorithm are the same as the ones coming out.

Once the divergence has dropped below some tolerance, typically a value of 10^{-7} or 10^{-10}, the algorithm is stopped.

3.4.1 Stability

In all, the model here presented has eleven parameters. All of these parameters have specific effects on the stability of the system which were investigated individually.

Six of these parameters are physical, relating to the potential and the macroscopic features of the system. These parameters are the total volume fraction f_A, the relative particle size α, the depth of the potential well A_1, the height of the potential barrier A_2, the width of the potential well λ, and the width of the potential barrier γ. The temperature k_BT has already been scaled out of the potential for convenience.

Five of the parameters are purely computational. They are the incompressibility parameter $\hat{\kappa}$, the mixing parameter ρ, the number of points on the lattice n^3, and the size of the system, taken to be a box of volume $V = L^3$.

The length of the box, the number of lattice points, and the two width parameters of the potential have a strong combined effect on stability. Should the box be too small, then finite size effects might wash out any of the interesting behaviour. Should it then be decided to make the box extremely large, the resolution of the lattice points would be far too big, washing out the subtleties of the morphologies and the potential. Increasing the size of the box would also cause the system to converge much more slowly or possibly fail to converge at all. Balancing these considerations, we chose a box length of approximately $L = 10$, with $n^3 = 262144$ lattice points for a potential with $\lambda = 2$ and $\gamma = 0.38$ by trial and error. With $\gamma > 2$, the excluded volume becomes too great, and the colloids essentially

have no room. Similarly as it approaches zero, the repulsive region begins to disappear and the colloids will macrophase separate. The width of the attractive region λ dictates how far apart the colloids should be before they will begin to feel repulsion. If $\lambda < 1$ then the attractive region is almost exclusively *within* the particle and there is no room for particles to aggregate. If $\lambda > 3$ then the interactions are too de-localized, happening far from the particles themselves.

The mixing parameter and the incompressibility parameter are also intimately related to stability. Should the incompressibility be too strong, then the region of density space that minimizes the free energy would be too small, the saddle point too "steep", causing the algorithm to never converge for any reasonable mixing parameter. Decreasing the mixing parameter to compensate would require too many iterations. It was found that $\kappa = 1000$ was sufficient to enforce incompressibility for the potentials of interest. To achieve this high incompressibility, $\rho = 0.001$ was found to be the largest mixing parameter which would achieve convergence.

3.4.2 Variable Incompressibility

In order to improve stability and speed convergence, a method was developed in which the incompressibility parameter $\hat{\kappa}$ and the mixing parameter ρ were varied strategically. It has been found that by keeping a lower incompressibility and a higher mixing parameter to create a "less steep" saddle point, and allowing the densities to converge, it is possible to use this density, assumed to be close to the fixed point, as an initial guess with an increased $\hat{\kappa}$ and decreased ρ.

For example, beginning with a κ of 10 and a ρ of 0.01, it is possible to achieve convergence relatively quickly, albeit to a density which may deviate from incompressibility. However, when κ is then turned up to 100 and ρ to 0.005, this density will converge much more quickly to a better estimate. Finally increasing κ to 1000 and ρ to 0.001, the system as a whole will have converged much faster, with a lower divergence measure than it would have otherwise. We refer to this method as the variable incompressibility method. Figure 3.2 compares the divergence as a function of iteration for a fixed incompressibility simulation versus a variable incompressibility simulation with identical physical parameters. After 100000 iterations, the divergence of the variable incompressibility simulation is 10^2 lower than that of the fixed incompressibility simulation.

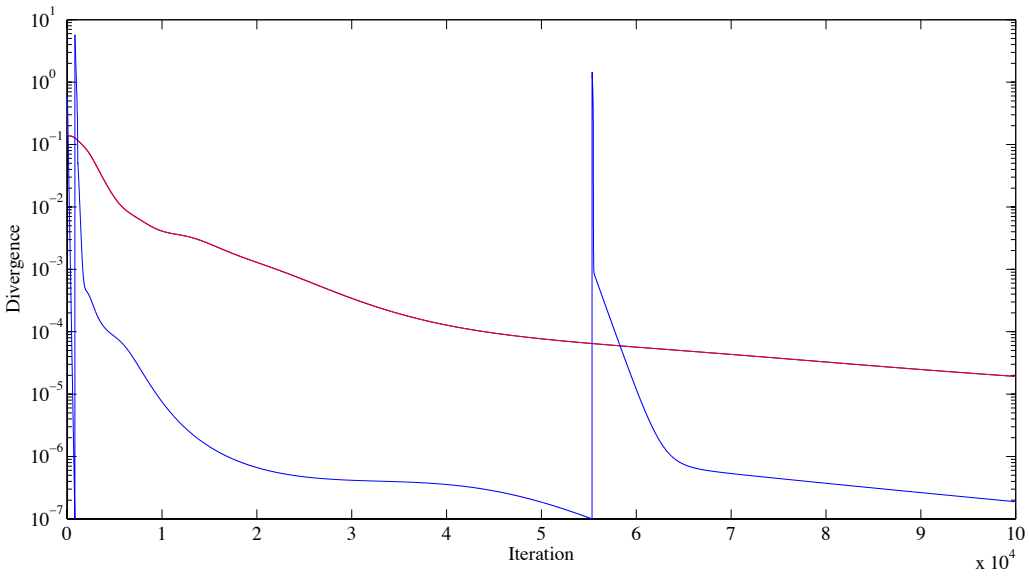

Figure 3.2: Comparison of the methods of fixed incompressibility versus variable incompressibility for systems with identical physical parameters in 1D. Using the fixed incompressibility method (red), the divergence decreases much more slowly with $\rho = 0.0005$ and $\hat{\kappa} = 1000$. Using the variable incompressibility method (blue), the divergence decreases to a lower value, also with a final $\rho = 0.0005$ and $\hat{\kappa} = 1000$. The spikes in the divergence correspond to the increases in incompressibility.

3.4.3 Density Functional Theory

The SCFT method was chosen for several reasons. In polymer physics, SCFT is well studied, allowing us a common formalism with a large body of research. Our approach is also easily scalable, allowing us to include many more particles species and interactions without a significant change to our framework.

Density Functional Theory (DFT) is an approach pioneered by Hohenberg and Kohn that creates a density function $\rho(\mathbf{r})$ defined everywhere in the system[23]. It should be noted that the ρ defined here is distinct from the mixing parameter introduced in Section 3.3. Beginning with our free energy in Equation 3.22, it is possible to algebraically reduce the free energy to just a density ϕ_A and ϕ_B functional.

While moving to a DFT version may be numerically more simple, the solutions may not be easier to obtain. Such an approach may be interesting but is beyond the scope of

this project.

Chapter 4

Results and Discussion

4.1 Potential and Dimensionality

In order to understand the relationship between the four parameters associated with the potential and the morphologies of the system, the parameters were varied while fixing $f_A = 0.5$ and $\alpha = 1$. This system, where the solvent and colloid particles are of equal size is unphysical but allowed for higher mixing parameters and faster convergence.

Our results in one-dimension served both as a proof of concept and allowed us to investigate the dependence of morphology on dimensionality for given parameters. Three phases were observed by varying the parameters of the potential. For infinite temperature where $A_1 = 0$ and $A_2 = 0$, the densities remained uniform (disordered) as expected. Fixing A_2, as we pass $A_1 > 2$, the densities begin to show signs of phase separation. By $A_1 > 4$, the densities have robustly phase separated, exhibiting macrophase separation as one would expect for a purely attractive potential. The A-species particle aggregation is moderated only by the incompressibility.

Conversely, fixing $A_1 = 0$ and varying A_2 has a different effect. For the most part, this results in a disordered phase. For simplicity, the γ parameter was replaced with the more intuitive Half Width at Half Maximum (HWHM) for the Gaussian portion of the potential. The relationship between these two parameters is HWHM $= \sqrt{\frac{\ln 2}{2}}\gamma$. Fixing HWHM $= 0.65$ while increasing the parameter A_2 results in a fairly rapid transition at $A_2 > 0.4$ to microphase separation. This phase manifests as a "dashed line" as illustrated in Figure 4.1, equivalent to a 1D cross section of a lamellar phase, and variations on this

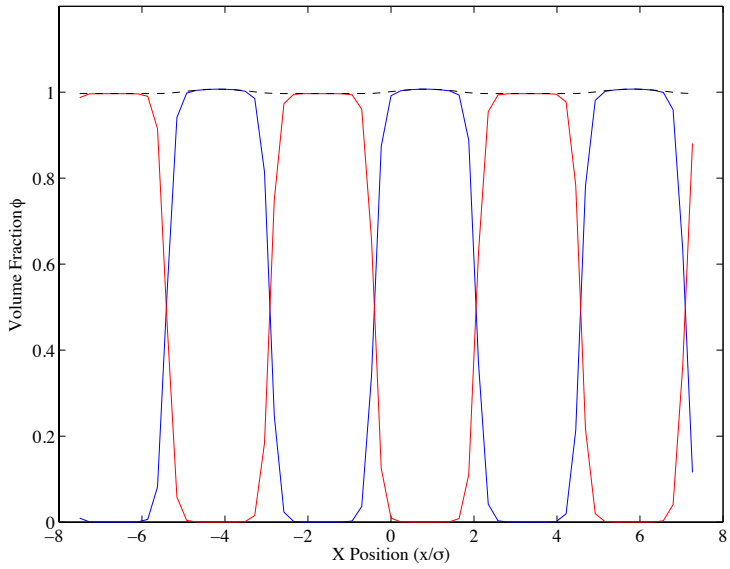

Figure 4.1: Plot of the density functions ϕ_A (blue) and ϕ_B (red) of a 1D system in a microphase separated phase. The "dashed line" morphology is the only microphase separated morphology available in 1D. Note that the system is strongly segregated, as the layers are either composed almost entirely either of A or B species particles.

are the only possible microphase separation in 1D. Turning up either A_1 or A_2 significantly higher simply led to a lack of stability.

In 2D, the possible morphologies become more interesting. Once again at high temperature, the A and B particles are distributed uniformly. As A_1 is increased, the system will macrophase separate beyond $A_1 > 2$. Fixing A_1 and increasing A_2, the system will begin to shift over to a striped morphology as $A_2 > 0.2$. Further decrease of temperature also led to instability. Figure 4.2 illustrates the microphase separated phases observed in 2D.

In 3D, similar behaviour was observed. $A_1 = A_2 = 0$ once again corresponds to a disordered phase. $A_1 > 0$ and $A_2 = 0$ corresponds to macrophase separation. Fixing $A_1 = 3$ and $A_2 = 0.3$ led to a lamellar morphology. We observed that the L region of the 2D system was significantly wider in terms of f_A than in 3D for the same potential. The 2D system would exhibit stripes until f_A decreased beyond 0.4, whereas by $f_A = 0.4$ in the 3D system, the system would have changed to a C phase.

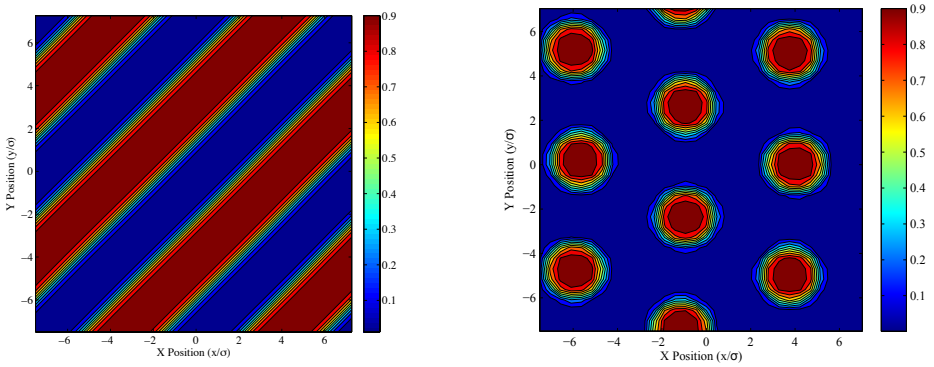

(a) 2D striped phase

(b) 2D cylinder phase

Figure 4.2: The results of 2D SCFT computation using $A_1 = 3$ and $A_2 = 0.3$. The colourbar represents the volume fraction ϕ_A. Figure (a) is the result of a calculation with $f_A = 0.5$. Figure (b) uses the same potential with $f_A = 0.2$.

4.2 Self-Assembly

4.2.1 Particle Size

We then focused entirely on the 3D system. With a potential in hand that produces lamellar morphologies at $L = 8$, $\alpha = 1$, HWHM $= 0.65$, $A_1 = 3$, and $A_2 = 0.3$, it was possible to fix the potential and investigate the morphologies by varying the total volume fraction f_A.

It was found that for fixed $\alpha = 1$ the phases exhibited a clear progression as f_A was decreased. Near $f_A = 0.5$, we found that the only possible phase was lamellar. From lamella, the progression was clear. For decreasing f_A, the lamella transition to cylindrical morphologies, then to spherical morphologies, followed finally by a disordered phase. In between the lamellar and cylindrical phases, we noticed a transitional phase of interest, which will be discussed later.

As previously discussed, α represents the relative particle volume as given by Equation 3.4. Since the A species particle in our model represents a colloidal particle and the B species particle represents solvent molecules, we are particularly interested in the small α regime $\alpha << 1$.

We repeated the procedure above at a lower temperature for fixed $\alpha = 0.1$. The

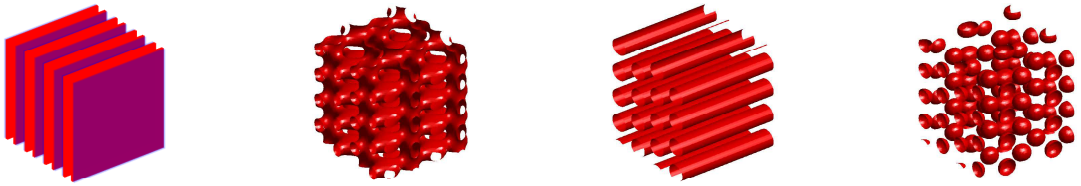

(a) Lamella (b) Gyroid (c) Cylinders (d) Spheres

Figure 4.3: The results of our 3D SCFT computation for $\alpha = 0.5$, HWHM $= 0.65$ and $L = 8$. The progression of phases observed as f_A is decreased from $f_A = 0.5$. From $f_A = 0.5$ to $f_A \approx 0.45$, Lamella (L) are observed (a). Near $f_A \approx 0.4$, the system moves to a Gyroid phase (b). From $f_A \approx 0.35$ to $f_A \approx 0.25$, the system enters a Cylindrical (C) phase (c). From $f_A \approx 0.2$ to $f_A \approx 0.15$, the system enters a Spherical (S) phase (d), before finally becoming disordered as $f_A < 0.15$. This result is very similar to the progression of phases for diblock copolymer melts while varying the same parameter. Note that these results were computed using an $L = 8$ sided box. The results have been tiled for clarity.

potential characterized by $A_1 = 11$, and $A_2 = 3$ was sufficient to produce a lamellar phase at $f_A = 0.5$. It was found that, although requiring a lower temperature, the system exhibited the same progression as it did for higher α. In addition, it also exhibited the same transitional phases going from lamella to cylinders. We noted that as α and f_a decreased, the mixing parameter ρ had to correspondingly decrease as well.

Extrapolating from the experiences above, it was finally possible to map the phases for $\alpha \approx 0.05$ and $\alpha \approx 0.01$ as a function of f_A, which correspond to more physical systems. These required yet another reduction of temperature and mixing parameter, and produced the same progression of phases as the previous systems. A potential characterized by $A_1 = 17$, and $A_2 = 5$ was chosen.

The dependence of phase on the particle size is to be expected. As particle size decreases, the entropic gain of a disordered system will dominate the energy gain of aggregation.

4.2.2 Temperature

In order to better understand the temperature dependence of the self-assembly, we performed several runs varying both temperature and total volume fraction f_A.

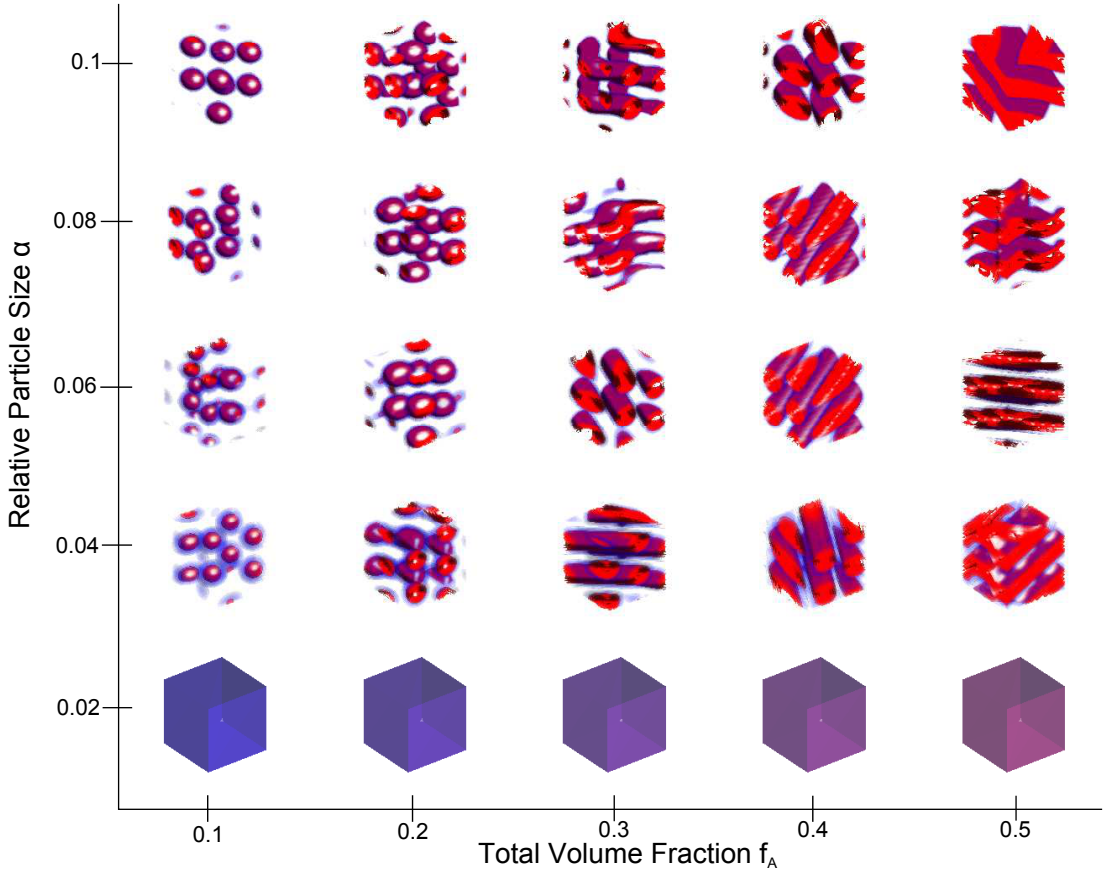

Figure 4.4: Phases of the system as a function of total volume fraction and particle size at fixed temperature using an isosurface of $\phi_A = 0.5$. The plot was computed using the Variable Incompressibility method with final $\rho = 0.0005$ and $\tilde{\kappa} = 900$. The purple region indicates the surface facing the solvent particle. The filled boxes indicate the disordered phase. Note the progression of the phases from L to S. The G phase is omitted from this plot, however it has been observed between $f_A = 0.5$ and $f_A = 0.4$ on higher resolution plots.

As expected, at high temperature, the system was in a disordered phase. The phases achieved as the temperature was dropped depended heavily on the total volume fraction. For $f_A \approx 0.5$, the system entered a lamellar phase. As the total volume fraction dropped, the system first entered a complex phase (PL or G) then moved to cylindrical, then spherical

before finally becoming disordered for small f_A.

We produced plots by fixing alpha and varying temperature T and total volume fraction f_A. We plotted the phases as a function of these two parameters. Fixing the ratio of A_1 to A_2, we scaled the temperature by a multiplicative factor. The maximum temperature was set using a potential characterized by $A_1 = 11$ and $A_2 = 3$. This was repeated for $\alpha = 0.05$ and $\alpha = 0.1$.

In the case of $\alpha = 0.1$, the system was unsurprisingly in a disordered state at high temperatures. As the temperature was decreased in the neighbourhood of $f_A \approx 0.5$, the system first macrophase separated, then as temperature decreased further began to move to an L phase. Near $f_A \approx 0.3$, the system moved from the disordered phase to first a macrophase separation then a cylindrical phase. Finally, for $f_A = 0.1$, the system moved directly from a disordered phase to an S phase.

In each case, both the divergence as well as the energy, given by Equation 3.22, was calculated along with the densities for comparison. For the same potential, two states with different free energies would imply that the higher of the two is likely a metastable state.

4.3 Comparison with Diblock Copolymer Melts

Perhaps the most striking agreement comes from the results of Matsen et al. Our results parallel their simulations of a diblock copolymer melt system. Comparing our progression of phases, seen in Figure 4.3, with the theoretical results reported by Matsen et al. reveals some striking similarities as shown in Figure 4.6. Their progression of phases [42], $L \to G \to C \to S$, shows strong agreement with our own as shown in Figure 4.5.

There are marked differences in the physics of our system and diblock copolymer systems. As previously discussed in Section 2.1, one of the more important properties of block copolymers is packing frustration. As previously discussed in Section 2.2, packing frustration is a result of the conflict between the interfacial and stretching energy terms of diblock copolymer systems. Packing frustration is an important consideration when examining the G, PL and D phases. Interestingly, our model does not include any connectivity between particles, thus does not have any packing frustration, yet exhibits a very similar progression of phases including a G phase.

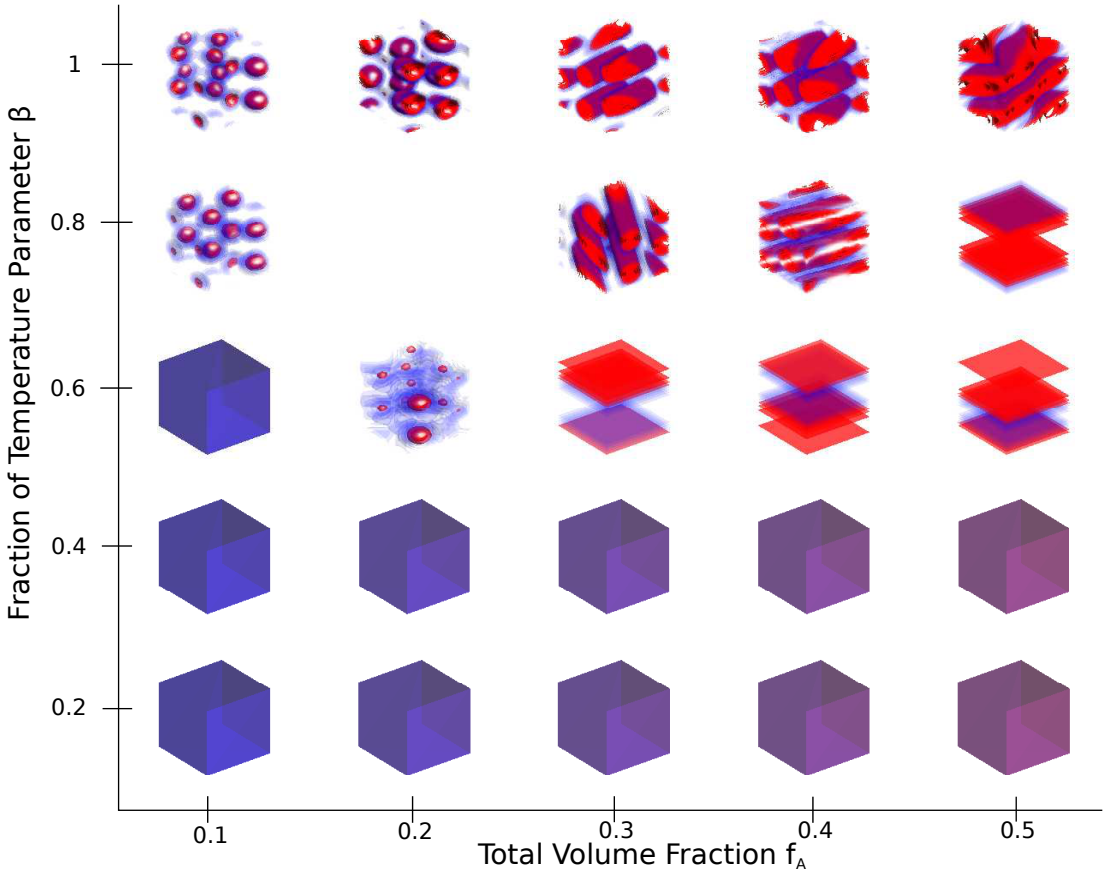

Figure 4.5: Phases of the system as a function of total volume fraction and temperature at fixed particle size $\alpha = 0.05$ using an isosurface of $\phi_A = 0.5$. The plot was computed using the Variable Incompressibility method with final $\rho = 0.0005$ and $\tilde{\kappa} = 900$. The purple region indicates the surface facing the solvent particle. The filled boxes indicate the disordered phase. It should be noted that the empty space is a simulation that failed to converge below the threshold divergence.

4.4 Improvements to SCFT

As a mean-field theory, SCFT has several notable shortfalls. As previously discussed, our mean-field approach does not take into account any fluctuations. As a result, some of the saddle points computed may not be physically significant [17]. For example, while a PL

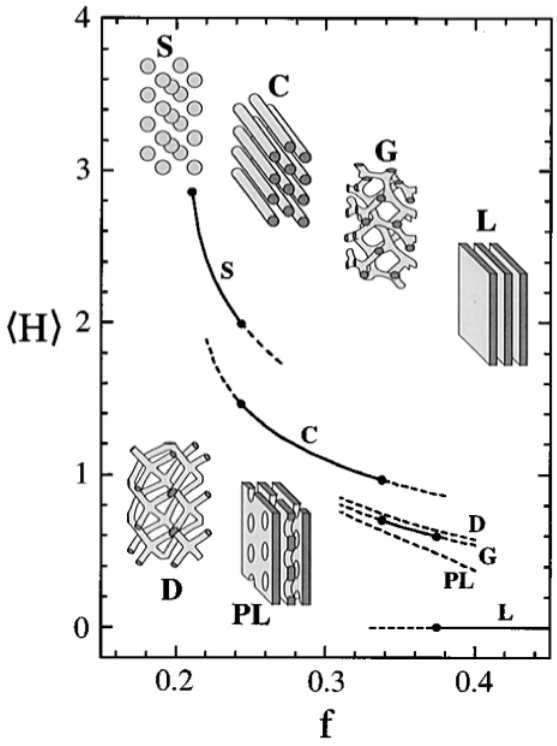

Figure 4.6: A theoretical plot of the mean curvature $< H >$ versus total volume fraction f of a diblock copolymer melt system. Solid lines indicate stability, while dashed lines indicate metastability. The plot illustrates the progression of stable phases as the total volume fraction is decreased. From Matsen and Bates [38].

phase may correspond to a saddle point, fluctuations may prevent this state from being observed due to its instability.

As suggested by Fredrickson et al., this project implements a method whereby each simulation is begun using a random seed. It can be reasonably assumed that using this method, for a large number of trials, that all of the relevant fixed points will be found [17]. Suspicions of metastability can also be verified by checking the free energies of a given set of states (under identical parameters, differing only in their initial random states) in order to determine if one state is significantly higher in energy. One must be careful employing this method, as factors such as the size and shape of the "box" may raise the free energy of a given morphology.

It is also possible to incorporate Gaussian fluctuations into an SCFT approach [46].

Fluctuations away from a metastable saddle function will wash out any unstable fixed points.

Chapter 5

Conclusions

Using self-consistent field-theory, we have shown that the system of particles, with an isotropic interaction characterized by a long-range repulsion and short-range attraction, is capable of self-assembly. We have mapped these phases as they vary with temperature, volume fraction and particle size and found striking similarities to diblock copolymer melt systems, despite the lack of connectivity and packing frustration in our model.

By varying the total volume fraction of our A species particle with respect to the B species particle, we have found that the system moves through an $L \rightarrow G \rightarrow C \rightarrow S$ phase progression. This same progression was observed in diblock copolymer melts as the total volume fraction of the A block was varied with respect to the B block.

We also mapped the phase progression of the system as a function of temperature. We have found that as it decreases from an infinite temperature, the system moves first from a disordered phase, then to a macrophase separated phase, then into a microphase separated morphology determined by the total volume fraction of species A relative to species B particles. This behaviour diverges from that of diblock copolymers, as those classes of systems are by construction not capable of macrophase separation.

While it was not possible in the scope of this project, there is much that can be done using the SCFT approach to modelling systems of particles with isotropic interactions. For example, while we have modelled a two-species system, it would be relatively simple to expand our self-consistent equations for multi-particle species systems. This would allow customized interactions between different types of colloidal particles. Beginning with our SCFT framework, it would also be possible to construct a density functional theory model, perhaps even allowing for more efficient computation. In this way, our approach allows much room for expansion into systems not covered in the scope this project.

APPENDICES

Appendix A

Derivation of mathematical theorems used in derivation and computation

A.1 Path Integrals

The path integral formalism, which was first refined by Feynman, is explained in Das[10] by beginning with a Quantum Mechanical treatment.

We must first begin with, using the Dirac bra-ket notation, with the position basis denoted $|x\rangle$. Since the position basis is a complete basis, we can use the property

$$\int dx \, |x\rangle \, \langle x| = I \tag{A.1}$$

which is also true in the Heisenberg picture

$$\int dx \, |x,t\rangle \, \langle x,t| = I \tag{A.2}$$

and since the basis states are orthonormal

$$\langle x|x'\rangle = \delta(x - x') \tag{A.3}$$

where I is the identity operator. Note that these properties are equally valid for the momentum basis $|p\rangle$.

Without going into extreme detail, Weyl ordering is a method of converting classical

commuting products into non-commuting operators. Weyl ordering simply symmetrizes all possible combinations with equal weight [10]. Thus, for example, the position and momentum operators can be reordered as

$$x^2 p \to \frac{1}{3}(x^2 p + xpx + px^2) \tag{A.4}$$

Applying Weyl ordering to the Hamiltonian, it can be shown that

$$\langle x|H^{WO}|x'\rangle = \int \frac{dp}{2\pi\hbar} e^{-\frac{i}{\hbar}p(x-x')} H\left(\frac{x+x'}{2}, p\right) \tag{A.5}$$

Next, let us define an infinitesimal length of time $\epsilon \equiv \frac{t_f - t_i}{N}$.

Now, it is possible to calculate the transition amplitude between some initial state and final state by repeatedly applying the completeness identity from Equation A.1.

$$\begin{aligned} U(x_i, t_i; x_f, x_f) &= \langle x_f, t_f | x_i, x_i\rangle & \text{(A.6)} \\ &= \lim_{N\to\infty} \int dx_1 ... dx_N \, \langle x_f, t_f | x_{N-1}, t_{N-1}\rangle \, ... \, \langle x_1, t_1 | x_i, t_i\rangle & \text{(A.7)} \end{aligned}$$

We now see that

$$\begin{aligned} \langle x_f, t_f | x_i, t_i\rangle &= \langle x_n | e^{-\frac{i}{\hbar}t_n H} e^{\frac{i}{\hbar}t_{n-1}H} | x_{n-1}\rangle & \text{(A.8)} \\ &= \langle x_n | e^{-\frac{i}{\hbar}\epsilon H} | x_{n-1}\rangle & \text{(A.9)} \\ &= \int \frac{dp_n}{2\pi\hbar} e^{\frac{i}{\hbar}p_n(x_n - x_{n-1}) - \frac{i}{\hbar}\epsilon H\left(\frac{x+x'}{2}, p\right)} & \text{(A.10)} \end{aligned}$$

Substituting a Hamiltonian of the form $H(x,p) = \frac{p^2}{2m} + V(x)$, we arrive at

$$U(x_i, t_i; x_f, x_f) = \lim_{N\to\infty} \left(\frac{m}{2\pi i\hbar\epsilon}\right)^{\frac{N}{2}} \int dx_1 ... dx_N e^{\frac{i\epsilon}{\hbar}\sum_{n=1}^{N}\left(\frac{m}{2}\left(\frac{x_n - x_{n-1}}{\epsilon}\right)^2 - V\left(\frac{x_n + x_{n-1}}{2}\right)\right)} \tag{A.11}$$

which can be rewritten as

$$U(x_i, t_i; x_f, x_f) = A \int \mathcal{D}x e^{\frac{i}{\hbar}S[x]} \tag{A.12}$$

The significance of this, as explained by Das, is that in this integral, the endpoints are

fixed while all intermediary points are integrated over all space [10]. This is equivalent to integrating over all possible paths, with each path weighted according to $\exp(\frac{i}{\hbar}S[x])$ [10].

In the classical limit, as $\hbar \to 0$, the phase factor becomes very large and therefore, with phases very near each other likely to have different signs, many paths will cancel each other. However, the paths near the classical path, which satisfies $\frac{\delta S[x]}{\delta x} = 0$, will contribute to the transition amplitude. Therefore, these paths will dominate [10].

A.2 The Saddle-Function Approximation

From Das [10], it is possible to use the results of Section A.1 to approximate a path integral. We argued that in the classical limit, the classical path is the path that satisfies

$$\left.\frac{\delta S[x]}{\delta x}\right|_{x=x_c} = 0 \tag{A.13}$$

where the c subscript denotes the classical path. Let us expand the action $S[x]$ about the classical trajectory by defining $x(t) \equiv x_c(t) + \eta(t)$. Therefore, we can write the Taylor expansion of the action about the classical path.

$$\begin{aligned} S[x] &= S[x_c + \eta] && \text{(A.14)} \\ &= S[x_c] + \frac{1}{2}\int\int dt_1 dt_2 \eta(t_1) \frac{\delta^2 S[x_c]}{\delta x_c(t_1)\delta x_c(t_2)} \eta(t_2) + O(\eta^3) && \text{(A.15)} \end{aligned}$$

Note that due to Equation A.13, the first order expansion is zero.

Referring back to the transition amplitude from Equation A.12, we can now integrate over all paths.

$$U(x_i, t_i; x_f, x_f) = A\int \mathcal{D}\eta e^{\frac{i}{\hbar}\left(S[x_c] + \frac{1}{2}\int\int dt_1 dt_2 \eta(t_1) \frac{\delta^2 S[x_c]}{\delta x_c(t_1)\delta x_c(t_2)} \eta(t_2) + O(\eta^3)\right)} \tag{A.16}$$

allowing us to approximate the transition amplitude using the classical trajectory [10].

$$U(x_i, t_i; x_f, x_f) \approx \frac{A}{\sqrt{\det\left(\frac{1}{\hbar}\frac{\delta^2 S[x_c]}{\delta x_c(t_1)\delta x_c(t_2)}\right)}} e^{\frac{i}{\hbar}S[x_c]} \tag{A.17}$$

A.3 Functional Derivatives

In order to compute the functional derivative of the free energy in Equation 3.22, it is necessary to begin with the definition of the functional derivative. The functional derivative, or Gateaux derivative [10], is given as given by

$$\frac{\delta F[f(x)]}{\delta f(y)} = \lim_{\epsilon \to 0} \frac{F[f(x) + \epsilon\delta(x-y)] - F[f(x)]}{\epsilon} \tag{A.18}$$

and is defined as the *functional derivative of functional F with respect to function f*. Using the above definition, it is possible to calculate the functional derivatives given in Equations 3.18 and 3.19.

A.4 The Convolution Theorem

From Riley et al. we find a proof of the convolution theorem. The proof is shown for functions of a single variable, but the theorem is easily extended to $\mathbb{R}^n$. The convolution of two functions f and g is given by

$$h(z) \equiv f(g(z)) = \int_{-\infty}^{+\infty} f(x)g(z-x)dx \tag{A.19}$$

Let us now take the Fourier transform of $h(z)$.

$$\begin{aligned} \tilde{h}(z) &= \int_{-\infty}^{+\infty} dz e^{-ikz} \left[\int_{-\infty}^{+\infty} f(x)g(z-x)dx \right] \\ &= \int_{-\infty}^{+\infty} f(x)dx \left[\int_{-\infty}^{+\infty} g(z-x)e^{-ikz}dz \right] \end{aligned} \tag{A.20}$$

Now let us define $u \equiv z - x$. The equation then becomes

$$\begin{aligned} \tilde{h}(z) &= \int_{-\infty}^{+\infty} f(x)dx \left[\int_{-\infty}^{+\infty} g(u)e^{-ik(u+x)}du \right] \\ &= \int_{-\infty}^{+\infty} f(x)e^{-ikx}dx \left[\int_{-\infty}^{+\infty} g(u)e^{-iku}du \right] \\ &= \tilde{f}(k)\tilde{g}(k) \end{aligned} \tag{A.21}$$

The converse can similarly be proven [53].

Appendix B

Notes on MATLAB Functions Used in the Computation

The following notes on MATLAB functions were made with the use of the MATLAB R2012a Documentation[...].

B.1 Notes on the Fast Fourier Transform

The Fourier transforms required to solve the self-consistent equations were accomplished using the MATLAB FFT and FFTN functions. These functions calculate the discrete Fourier transforms of a vector of length N and an array of N^d respectively.

Let us define $w_N \equiv \exp(-2\pi i/N)$. Using the FFT function in MATLAB on the vector x of length N is equivalent to applying

$$X(k) = \sum_{j=1}^{N} x(j) w_N^{(j-1)(k-1)} \tag{B.1}$$

with the inverse Fourier transform IFFT equivalent to

$$x(j) = \frac{1}{N} \sum_{k=1}^{N} X(k) w_N^{-(j-1)(k-1)} \tag{B.2}$$

Higher dimensional calculations required the use of the MATLAB functions FFTN and

IFFTN. From the MATLAB documentation, using the FFTN function is equivalent to applying

```
Y = X;
for p = 1:length(size(X))
    Y = fft(Y,[],p);
end
```

where SIZE(X) returns the number of elements in each dimension of the array X. Should d-dimensional array X have N^d elements, SIZE(X) would return the vector $[NN...N]$ of length d. The function LENGTH(Z) returns the number of elements in the largest dimension of an array. For the vector $Z = [NN...N]$ of length d, the function LENGTH(Z) would return d.

The above code calculates the Fourier transform using FFT by applying it to each dimension in sequence.

B.2 Notes on the Random Number Generator

The MATLAB RANDN function was used in order to randomly generate the initial density function, as described in Section 3.3. This function generates random number based on the Normal (Gaussian) distribution.

In order to improve the random number generation, the MATLAB random number generator (RandStream) was initialized using the "shuffle" command. This ensured that the number stream was seeded using the system clock.

Appendix C

The MATLAB Code Used in the Project

```
clear

fa_min = 0.1;
fa_max = 0.5;
fa_step = 0.1;
T_min = 0.2;
T_max = 1;
T_step = 0.2;

alpha = 0.05;
maxn = 3;

kappa = [10 100 900];
mix = [0.01 0.005 0.00005];

iter = 200000;
tol = 10^(-7);
mj = 64;
mk = 64;
ml = 64;
xsize = 8; %8, 10, 15
ysize = 8;
```

```
zsize = 8;

initA1 = 11; %3.00, 11, 17
initA2 = 3; %0.30, 3, 5
lambda = 2;
HWHM = 0.65;

for n = 1:maxn
    for fa = fa_min:fa_step:fa_max
        for T = T_min:T_step:T_max
            fb = 1 - fa;
            A1 = T*initA1;
            A2 = T*initA2;
            outfile = strcat('fa',num2str(fa),'T',num2str(T),'A1'
                ,num2str(A1),'A2',num2str(A2));
            paroutfile = strcat(outfile,'_',num2str(n),'_par.mat'
                );
            feoutfile = strcat('/work/kvonkoni/orca/alpha0.05xs8_
                ',num2str(n),'/',outfile,'_fe.mat');
            outfile = strcat('/work/kvonkoni/orca/alpha0.05xs8_',
               num2str(n),'/',outfile,'.mat');
            save(paroutfile);
        end
    end
end

clear

parfile = input('Parameter file: ','s')
load(parfile);

hmj = mj/2;
hmk = mk/2;
hml = ml/2;
dx = xsize/mj;
dy = ysize/mk;
dz = zsize/ml;
xxs=-xsize/2:dx:(xsize/2-dx);
```

```
yys=-ysize/2:dy:(ysize/2-dy);
zzs=-zsize/2:dz:(zsize/2-dz);

shift = zeros(1,numel(kappa));

Vaa = zeros(mj,mk,ml);
Vbb = zeros(mj,mk,ml);
Vab = zeros(mj,mk,ml);
gamma = HWHM/sqrt(2*log(2));
for j=1:mj
    for k=1:mk
        for l=1:ml
            r = sqrt(xxs(j)^2+yys(k)^2+zzs(l)^2);
            if r<=lambda
                Vaa(j,k,l) = -(A1+A2)*cos(pi*r/lambda)/2-(A1-A2)
                    /2;
            else
                Vaa(j,k,l) = A2*exp(-(r-lambda)^2/(2*gamma^2));
            end
        end
    end
end

Vaa = circshift(Vaa,[hmj hmk 0]);
Vbb = circshift(Vbb,[hmj hmk 0]);
Vab = circshift(Vab,[hmj hmk 0]);

Vka = fftn(Vaa)./(mj*mk*ml);
Vkb = fftn(Vbb)./(mj*mk*ml);
Vkm = fftn(Vab)./(mj*mk*ml);

% Load from file.
%{
file = load('drift_check.mat');
phia = file.phia;
phib = file.phib;
%}
```

```
rng('shuffle');
std = 0.15;
phia = fa + std.*randn(mj,mk,ml);
phib = 1 - phia;

g=1;
for h=1:numel(kappa)
    for i=1:iter

        iphia = fftn(phia);
        iphib = fftn(phib);

        cnva = iphia.*Vka;
        cnvb = iphib.*Vkb;
        cnvma = iphib.*Vkm;
        cnvmb = iphia.*Vkm;

        icnva = xsize*ysize*zsize*ifftn(cnva);
        icnvb = xsize*ysize*zsize*ifftn(cnvb);
        icnvma = xsize*ysize*zsize*ifftn(cnvma);
        icnvmb = xsize*ysize*zsize*ifftn(cnvmb);

        wa = icnva+icnvma-kappa(h).*(1-phia-phib);
        wb = icnvb+icnvmb-kappa(h).*(1-phia-phib);

        ewa = exp(-wa);
        ewb = exp(-alpha*wb);
        QA = dx*dy*dz*sum(sum(sum(ewa)));
        if isnan(QA)
            error('Q is NaN');
        end
        QB = dx*dy*dz*sum(sum(sum(ewb)));

        phiatemp = fa*xsize*ysize*zsize*ewa/QA;
        phibtemp = fb*xsize*ysize*zsize*ewb/QB;

        phiaave = fa-dx*dy*dz*sum(sum(sum(phiatemp)))/(xsize*
            ysize*zsize);
```

```
        phibave = fb-dx*dy*dz*sum(sum(sum(phibtemp)))/(xsize*
            ysize*zsize);

        phianew = phiatemp+phiaave;
        phibnew = phibtemp+phibave;

        phia = mix(h)*phianew+(1-mix(h))*phia;
        phib = mix(h)*phibnew+(1-mix(h))*phib;

        max_phi_tot = max(max(max(phia+phib)));
        min_phi_tot = min(min(min(phia+phib)));

        dev = phianew-phia;
        dev2 = dev.*dev;
        norm = sum(sum(sum(phianew.*phianew)));
        phidev(g) = sum(sum(sum(dev2)))/norm;

        if phidev(g) < tol
            shift(h) = g;
            break;
        end
        g=g+1;
    end
end

iphia = fftn(phia);
iphib = fftn(phib);

iphiaVka = iphia.*Vka;
iphibVkb = iphib.*Vkb;
iphiaVkm = iphia.*Vkm;

phiaVphia = (xsize*ysize*zsize)*ifftn(iphiaVka).*phia;
phibVphib = (xsize*ysize*zsize)*ifftn(iphibVkb).*phib;
phiaVphib = (xsize*ysize*zsize)*ifftn(iphiaVkm).*phib;

iwa = fftn(wa);
iwb = fftn(wb);
```

```
iwaiphia = iwa.*iphia;
iwbiphib = iwb.*iphib;

waphia = (xsize*ysize*zsize)*ifftn(iwaiphia);
wbphib = (xsize*ysize*zsize)*ifftn(iwbiphib);

comprss = phia+phib-ones(mj,mk,ml);
comprss2 = comprss.^2;

F = -fa*log(QA)-(fb/alpha)*log(QB)+dx*dy*dz*sum(sum(sum(phiaVphia
    )))/(2*xsize*ysize*zsize)+dx*dy*dz*sum(sum(sum(phiaVphib)))/(
    xsize*ysize*zsize)+dx*dy*dz*sum(sum(sum(phibVphib)))/(2*xsize*
    ysize*zsize)-dx*dy*dz*sum(sum(sum(waphia)))/(xsize*ysize*zsize
    )-dx*dy*dz*sum(sum(sum(wbphib)))/(xsize*ysize*zsize)+(kappa(
    end)/2)*dx*dy*dz*sum(sum(sum(comprss2)))

last_phidev = phidev(end)

phimax = max(max(max(phia+phib)))
phimin = min(min(min(phia+phib)))

phiamin = min(min(min(phia)))
phibmin = min(min(min(phib)))

if exist('alpha_max','var')
    save(outfile,'phia','phib','F','fa','alpha','A1','A2','HWHM',
        'lambda','xsize','ysize','zsize','alpha_max','alpha_min','
        alpha_step','fa_max','fa_min','fa_step','last_phidev');
elseif exist('T_max','var')
    save(outfile,'phia','phib','F','fa','alpha','A1','A2','T','
       HWHM','lambda','xsize','ysize','zsize','T_max','T_min','
        T_step','fa_max','fa_min','fa_step','last_phidev');
elseif exist('A1_max','var')
    save(outfile,'phia','phib','F','fa','alpha','A1','A2','HWHM',
        'lambda','xsize','ysize','zsize','A2_max','A2_min','
        A2_step','A1_max','A1_min','A1_step','last_phidev');
else
```

```
    save(outfile);
end
```

References

[1] Pinar Akcora, Hongjun Liu, Sanat K. Kumar, Joseph Moll, Yu Li, Brian C. Benicewicz, Linda S. Schadler, Devrim Acehan, Athanassios Z. Panagiotopoulos, Victor Pryamitsyn, Venkat Ganesan, Jan Ilavsky, Pappanan Thiyagarajan, Ralph H. Colby, and Jack F. Douglas. Anisotropic self-assembly of spherical polymer-grafted nanoparticles. *Nature materials*, 8(4):354–9, April 2009.

[2] Daniel J. Amit. *Field Theory, the Renormalization Group, and Critical Phenomena*. McGraw-Hill, 1978.

[3] T. M. Beardsley and Mark W. Matsen. Monte Carlo phase diagram for diblock copolymer melts. *The European physical journal. E, Soft matter*, 32(3):255–64, July 2010.

[4] T. M. Beardsley and Mark W. Matsen. Monte Carlo Phase Diagram for a Polydisperse Diblock Copolymer Melt. *Macromolecules*, 44(15):6209–6219, August 2011.

[5] Adi Ben-Israel. A Newton-Raphson method for the solution of systems of equations. *Journal of Mathematical Analysis and Applications*, 15(2):243–252, August 1966.

[6] Pawe Bryk and Luis G. Macdowell. Self-consistent field/density functional study of conformational properties of polymers at interfaces: role of intramolecular interactions. *The Journal of chemical physics*, 129(10):104901, September 2008.

[7] Sergey V. Buldyrev, Gianpietro Malescio, C. A. Angell, N. Giovambattista, S. Prestipino, F. Saija, H. Eugene Stanley, and L. Xu. Unusual phase behavior of one-component systems with two-scale isotropic interactions. *Journal of Physics: Condensed Matter*, 21(50):504106, December 2009.

[8] R. Car. Unified Approach for Molecular Dynamics and Density-Functional Theory. *Physical Review Letters*, 55(22):2471–2474, November 1985.

[9] David Chandler. *Introduction to Modern Statistical Mechanics*. Oxford University Press, 1987.

[10] Ashok Das. *Field Theory: A Path Integral Approach*. World Scientific, 1993.

[11] Rémi Dreyfus, Mirjam E. Leunissen, Roujie Sha, Alexei Tkachenko, Nadrian C. Seeman, David J. Pine, and Paul M. Chaikin. Aggregation-disaggregation transition of DNA-coated colloids: Experiments and theory. *Physical Review E*, 81(4):1–10, April 2010.

[12] C. Ebner, W. Saam, and D. Stroud. Density-functional theory of simple classical fluids. I. Surfaces. *Physical Review A*, 14(6):2264–2273, December 1976.

[13] S. F. Edwards. The statistical mechanics of polymers with excluded volume. *Proceedings of the Physical Society*, 85(4):613–624, April 1965.

[14] S. A. Egorov. Sterically stabilized lock and key colloids: a self-consistent field theory study. *The Journal of chemical physics*, 134(19):194901, May 2011.

[15] J. G. E. M. Fraaije and G. J. A. Sevink. Model for Pattern Formation in Polymer Surfactant Nanodroplets. *Macromolecules*, 36(21):7891–7893, October 2003.

[16] Glenn H. Fredrickson. Computational field theory of polymers: opportunities and challenges. *Soft Matter*, 3(11):1329, 2007.

[17] Glenn H. Fredrickson, Venkat Ganesan, and François Drolet. Field-Theoretic Computer Simulation Methods for Polymers and Complex Fluids. *Macromolecules*, 35(1):16–39, January 2002.

[18] Daan Frenkel and David J. Wales. Colloidal self-assembly: designed to yield. *Nature materials*, 10(6):410–1, June 2011.

[19] Sharon C. Glotzer and Michael J. Solomon. Anisotropy of building blocks and their assembly into complex structures. *Nature materials*, 6(8):557–62, August 2007.

[20] Guy H. Griffiths, Bart Vorselaars, and Mark W. Matsen. Unit-Cell Approximation for DiblockCopolymer Brushes Grafted to Spherical Particles. *Macromolecules*, 44(9):3649–3655, May 2011.

[21] O. Gunnarsson. Density functional theory and molecular bonding. I. First-row diatomic molecules. *The Journal of Chemical Physics*, 67(9):3970, 1999.

[22] Tobias Hanrath. Colloidal nanocrystal quantum dot assemblies as artificial solids. *Journal of Vacuum Science & Technology A: Vacuum, Surfaces, and Films*, 30(3):030802, 2012.

[23] P. Hohenberg and W. Kohn. Inhomogeneous Electron Gas. *Physical Review*, 136(3B):B864–B871, November 1964.

[24] Su-Mi Hur, Carlos J. Garcia-Cervera, Edward J. Kramer, and Glenn H. Fredrickson. SCFT Simulations of Thin Film Blends of Block Copolymer and Homopolymer Laterally Confined in a Square Well. *Macromolecules*, 42(15):5861–5872, August 2009.

[25] Jaeup U. Kim and Mark W. Matsen. Interaction between Polymer-Grafted Particles. *Macromolecules*, 41(12):4435–4443, June 2008.

[26] Seung Ha Kim and Eric W. Cochran. Localization of spherical nanoparticles within lamellar AB diblock copolymer melts through self-consistent field theory. *Polymer*, 52(10):2328–2339, May 2011.

[27] Y.-F Lam and J. D. McPherson. An iterative procedure for solving nonlinear equations. *Journal of Mathematical Analysis and Applications*, 58(3):578–604, May 1977.

[28] Henk N. W. Lekkerkerker and Remco Tuinier. *Colloids and the depletion interaction*. Springer, 2011.

[29] S. V. Lishchuk. Self-consistent field theory simulation of block copolymer films adsorbed on surfaces of azimuthally symmetric particles. *Journal of Physics A: Mathematical and Theoretical*, 42(46):465401, November 2009.

[30] Robert J. Macfarlane, Byeongdu Lee, Haley D. Hill, Andrew J. Senesi, Soenke Seifert, and Chad A. Mirkin. Molecular recognition and self-assembly special feature: Assembly and organization processes in DNA-directed colloidal crystallization. *Proceedings of the National Academy of Sciences of the United States of America*, 106(26):10493–8, June 2009.

[31] Robert J. Macfarlane, Byeongdu Lee, Matthew R. Jones, Nadine Harris, George C. Schatz, and Chad A. Mirkin. Nanoparticle superlattice engineering with DNA. *Science (New York, N.Y.)*, 334(6053):204–8, October 2011.

[32] Gianpietro Malescio, Giancarlo Franzese, Anna Skibinsky, Sergey V. Buldyrev, and H. Eugene Stanley. Liquid-liquid phase transition for an attractive isotropic potential with wide repulsive range. *Physical Review E*, 71(6):1–8, June 2005.

[33] Francisco Martinez-Veracoechea, Bianca Mladek, Alexei Tkachenko, and Daan Frenkel. Design Rule for Colloidal Crystals of DNA-Functionalized Particles. *Physical Review Letters*, 107(4):10–13, July 2011.

[34] Mark W. Matsen. The standard Gaussian model for block copolymer melts. *Journal of Physics: Condensed Matter*, 14(2):R21–R47, January 2002.

[35] Mark W. Matsen. New Fast SCFT Algorithm Applied to Binary Diblock Copolymer/Homopolymer Blends. *Macromolecules*, 36(25):9647–9657, December 2003.

[36] Mark W. Matsen. Self-Consistent Field Theory and Its Applications by M. W. Matsen. In Gerhard Gompper and Michael Schick, editors, *Soft Matter Vol. 1: Polymer Melts and Mixtures*, volume 1 of *Soft Matter*, chapter 2. Wiley-VCH Verlag GmbH & Co. KGaA, Weinheim, Germany, December 2005.

[37] Mark W. Matsen. Effect of Architecture on the Phase Behavior of AB-Type Block Copolymer Melts. *Macromolecules*, 45(4):2161–2165, February 2012.

[38] Mark W. Matsen and F. S. Bates. Origins of Complex Self-Assembly in Block Copolymers. *Macromolecules*, 29(23):7641–7644, January 1996.

[39] Mark W. Matsen, Guy H. Griffiths, R. A. Wickham, and O. N. Vassiliev. Monte Carlo phase diagram for diblock copolymer melts. *The Journal of chemical physics*, 124(2):024904, January 2006.

[40] Mark W. Matsen and Michael Schick. Stable and unstable phases of a diblock copolymer melt. *Physical Review Letters*, 72(16):2660–2663, April 1994.

[41] Mark W. Matsen and Michael Schick. Stable and Unstable Phases of a Linear Multiblock Copolymer Melt. *Macromolecules*, 27(24):7157–7163, November 1994.

[42] Mark W. Matsen and Michael Schick. Self-assembly of block copolymers. *Current Opinion in Colloid & Interface Science*, 1(3):329–336, June 1996.

[43] Guangnan Meng, Natalie Arkus, Michael P. Brenner, and Vinothan N. Manoharan. The free-energy landscape of clusters of attractive hard spheres. *Science (New York, N.Y.)*, 327(5965):560–3, January 2010.

[44] Chad A. Mirkin, R. L. Letsinger, R. C. Mucic, and J. J. Storhoff. A DNA-based method for rationally assembling nanoparticles into macroscopic materials. *Nature*, 382(6592):607–9, August 1996.

[45] Marcus Mueller. Computational Approaches for Structure Formation in Multicomponent Polymer Melts. In *Modeling and Simulation in Polymers*. Wiley, 2010.

[46] Marcus Mueller and Friederike Schmid. Incorporating fluctuations and dynamics in self-consistent field theories for polymer blends. *Advances in Polymer Science*, 185:1–58, January 2005.

[47] J. R. Naughton and Mark W. Matsen. Limitations of the Dilution Approximation for Concentrated Block Copolymer/Solvent Mixtures. *Macromolecules*, 35(14):5688–5696, July 2002.

[48] Benjamin M. D. ODriscoll, Guy H. Griffiths, Mark W. Matsen, and Ian W. Hamley. Structure Variation and Evolution in Microphase-Separated Grafted Diblock Copolymer Films. *Macromolecules*, 44(21):8527–8536, November 2011.

[49] Takao Ohta, Miho Motoyama, and Aya Ito. The kinetics and morphology of phase-separating copolymer mixtures. *Journal of Physics: Condensed Matter*, 8(25A):A65–A80, June 1996.

[50] Suchetan Pal, Zhengtao Deng, Haining Wang, Shengli Zou, Yan Liu, and Hao Yan. DNA directed self-assembly of anisotropic plasmonic nanostructures. *Journal of the American Chemical Society*, 133(44):17606–9, November 2011.

[51] Victor Pryamtisyn, Venkat Ganesan, Athanassios Z. Panagiotopoulos, Hongjun Liu, and Sanat K. Kumar. Modeling the anisotropic self-assembly of spherical polymer-grafted nanoparticles. *The Journal of chemical physics*, 131(22):221102, December 2009.

[52] L. E. Reichl. *Modern Course in Statistical Physics*. University of Texas Press, 1980.

[53] K. F. Riley, M. P. Hobson, and S. J. Bence. *Mathematical Methods for Physics and Engineering*. Cambridge University Press, Cambridge, 3rd edition, 2006.

[54] Jiunn-Ren Roan. Attraction between Nanoparticles Induced by End-Grafted Homopolymers in Good Solvent. *Physical Review Letters*, 86(5):1027–1030, July 2001.

[55] Jiunn-ren Roan. Self-consistent-field theory for spherical polymeric assemblies and its applications. *International Journal of Modern Physics B*, 18(17-19):2469–2475, 2004.

[56] S. Sacanna, W. T. M. Irvine, Paul M. Chaikin, and David J. Pine. Lock and key colloids. *Nature*, 464(7288):575–578, 2010.

[57] Raynaldo T. Scarlett, Marie T. Ung, John C. Crocker, and Talid Sinno. A mechanistic view of binary colloidal superlattice formation using DNA-directed interactions. *Soft Matter*, 7(5):1912, 2011.

[58] Dazhi Sun and Oleg Gang. Binary heterogeneous superlattices assembled from quantum dots and gold nanoparticles with DNA. *Journal of the American Chemical Society*, 133(14):5252–4, April 2011.

[59] Sabu Thomas, Charef Harrats, and Gabriel Groeninckx. Micro- and Nanostructured Polymer Blends: State of the Art, Challenges, and Future Prospects. In *Micro- and Nanostructured Multiphase Polymer Blend Systems: Phase Morphology and Systems*. CRC Press, 2006.

[60] Russell B. Thompson. Predicting nonpolymeric materials structure with real-space self-consistent field theory. *Physical Review E*, 73(2):2–5, February 2006.

[61] Russell B. Thompson, Valeriy V. Ginzburg, Mark W. Matsen, and Anna C. Balazs. Predicting the mesophases of copolymer-nanoparticle composites. *Science (New York, N.Y.)*, 292(5526):2469–72, June 2001.

[62] Russell B. Thompson, Valeriy V. Ginzburg, Mark W. Matsen, and Anna C. Balazs. Block Copolymer-Directed Assembly of Nanoparticles: Forming Mesoscopically Ordered Hybrid Materials. *Macromolecules*, 35(3):1060–1071, January 2002.

[63] Russell B. Thompson, K. Ø. Rasmussen, and T. Lookman. Improved convergence in block copolymer self-consistent field theory by Anderson mixing. *The Journal of chemical physics*, 120(1):31–4, January 2004.

[64] Russell B. Thompson, K. Ø. Rasmussen, and T. Lookman. Origins of Elastic Properties in Ordered Block Copolymer/Nanoparticle Composites. *Nano Letters*, 4(12):2455–2459, December 2004.

[65] Simon Tindemans and Bela Mulder. Designing colloidal ground-state patterns using short-range isotropic interactions. *Physical Review E*, 82(2):1–10, August 2010.

[66] Fernando Vargas Lara and Francis W. Starr. Stability of DNA-linked nanoparticle crystals I: Effect of linker sequence and length. *Soft Matter*, 7(5):2085, 2011.

[67] Bart Vorselaars, Jaeup U. Kim, Tanya L. Chantawansri, Glenn H. Fredrickson, and Mark W. Matsen. Self-consistent field theory for diblock copolymers grafted to a sphere. *Soft Matter*, 7(11):5128–5137, 2011.

[68] Qiang Wang and Yuhua Yin. Fast off-lattice Monte Carlo simulations with soft repulsive potentials. *The Journal of Chemical Physics*, 130(10):104903, 2009.

[69] MD Whitmore and JD Vavasour. Self-consistent field theory of block copolymers and block copolymer blends. *Acta polymerica*, pages 341–360, 1995.

[70] X. F. Yuan and A. J. Masters. Monte Carlo simulation and self-consistent field theory for a single block copolymer chain in selective solvents. *Polymer*, 38(2):339–346, January 1997.